

This work was written as part of one of the author's official duties as an Employee of the United States Government and is therefore a work of the United States Government. In accordance with 17 U.S.C. 105, no copyright protection is available for such works under U.S. Law.

Public Domain Mark 1.0

<https://creativecommons.org/publicdomain/mark/1.0/>

Access to this work was provided by the University of Maryland, Baltimore County (UMBC) ScholarWorks@UMBC digital repository on the Maryland Shared Open Access (MD-SOAR) platform.

Please provide feedback

Please support the ScholarWorks@UMBC repository by emailing scholarworks-group@umbc.edu and telling us what having access to this work means to you and why it's important to you. Thank you.

RESEARCH ARTICLE

10.1002/2017JD027412

This article is a companion
to Lee et al. (2017),
<https://doi.org/10.1002/2017JD027258>.

Key Points:

- VIIRS can be used to extend EOS-era aerosol data records to the NPP/Joint Polar Satellite System (JPSS) era, providing continuity as existing satellite missions end
- Results show improved capabilities to identify aerosol type and fine/coarse-mode partition, as compared to SeaWiFS and MODIS
- The data will be provided in near-real time alongside land Deep Blue data, to provide near-global coverage, for routine and research applications

Correspondence to:

A. M. Sayer,
andrew.sayer@nasa.gov

Citation:

Sayer, A. M., Hsu, N. C., Lee, J., Bettenhausen, C., Kim, W. V., & Smirnov, A. (2018). Satellite Ocean Aerosol Retrieval (SOAR) algorithm extension to S-NPP VIIRS as part of the "Deep Blue" aerosol project. *Journal of Geophysical Research: Atmospheres*, 123, 380–400. <https://doi.org/10.1002/2017JD027412>

Received 7 JUL 2017

Accepted 10 NOV 2017

Accepted article online 17 NOV 2017

Published online 4 JAN 2018

Satellite Ocean Aerosol Retrieval (SOAR) Algorithm Extension to S-NPP VIIRS as Part of the "Deep Blue" Aerosol Project

A. M. Sayer^{1,2} , N. C. Hsu² , J. Lee^{2,3} , C. Bettenhausen^{2,4}, W. V. Kim^{2,3} , and A. Smirnov^{2,5} 

¹Goddard Earth Sciences Technology and Research, Universities Space Research Association, Columbia, MD, USA, ²NASA Goddard Space Flight Center, Greenbelt, MD, USA, ³Earth Systems Science Interdisciplinary Center, University of Maryland, College Park, MD, USA, ⁴ADNET Systems Inc., Bethesda, MD, USA, ⁵Science Systems and Applications, Inc., Lanham, MD, USA

Abstract The Suomi National Polar-Orbiting Partnership (S-NPP) satellite, launched in late 2011, carries the Visible Infrared Imaging Radiometer Suite (VIIRS) and several other instruments. VIIRS has similar characteristics to prior satellite sensors used for aerosol optical depth (AOD) retrieval, allowing the continuation of space-based aerosol data records. The Deep Blue algorithm has previously been applied to retrieve AOD from Sea-viewing Wide Field-of-view Sensor (SeaWiFS) and Moderate Resolution Imaging Spectroradiometer (MODIS) measurements over land. The SeaWiFS Deep Blue data set also included a SeaWiFS Ocean Aerosol Retrieval (SOAR) algorithm to cover water surfaces. As part of NASA's VIIRS data processing, Deep Blue is being applied to VIIRS data over land, and SOAR has been adapted from SeaWiFS to VIIRS for use over water surfaces. This study describes SOAR as applied in version 1 of NASA's S-NPP VIIRS Deep Blue data product suite. Several advances have been made since the SeaWiFS application, as well as changes to make use of the broader spectral range of VIIRS. A preliminary validation against Maritime Aerosol Network (MAN) measurements suggests a typical uncertainty on retrieved 550 nm AOD of order $\pm(0.03+10\%)$, comparable to existing SeaWiFS/MODIS aerosol data products. Retrieved Ångström exponent and fine-mode AOD fraction are also well correlated with MAN data, with small biases and uncertainty similar to or better than SeaWiFS/MODIS products.

Plain Language Summary Aerosols are small particles in the atmosphere like desert dust, volcanic ash, smoke, industrial haze, and sea spray. Understanding them is important for applications such as hazard avoidance, air quality and human health, and climate studies. Satellite instruments provide an important tool to study aerosol loading over the world. However, individual satellites do not last forever and newer satellites often have improved capabilities compared to older ones. This paper describes and evaluates an extension of an algorithm, originally designed to monitor aerosols from an older satellite instrument, to a new satellite instrument called VIIRS.

1. Introduction

The Suomi National Polar-Orbiting Partnership (S-NPP) satellite was launched in late 2011, carrying a complement of five instruments for monitoring the Earth from space. S-NPP is a precursor to a series of operational satellites to be launched by the United States as part of its Joint Polar Satellite System (JPSS), the first of which is expected to launch in November 2017. The instruments aboard S-NPP and the JPSS satellites have been designed to be able to continue the types of observations made by the earlier Defense Meteorological Satellite Program (DMSP) and Earth Observing System (EOS) platforms; one of these instruments is the Visible Infrared Imaging Radiometer Suite (VIIRS; Cao et al., 2014, 2013), which draws from the heritage of instruments such as the Advanced Very High Resolution Radiometers (AVHRR), Sea-viewing Wide Field-of-view Sensor (SeaWiFS), and Moderate Resolution Imaging Spectroradiometers (MODIS). These DMSP and EOS instruments have been used widely for a broad variety of Earth science applications, including the study of tropospheric aerosols. Aerosol data products from these sensors have been created using a number of algorithms over both land (e.g., Hsu et al., 2004; Levy et al., 2007; Lyapustin et al., 2011) and water (e.g., Ahmad et al., 2010; Mishchenko et al., 1999; Sayer, Hsu, Bettenhausen, Ahmad, et al., 2012; Stowe et al., 1997; Tanré et al., 1997) surfaces and have been largely (although not exclusively) generated by or with the support of the U.S.'s National

Aeronautics and Space Administration (NASA). These data products have their individual strength and weaknesses, due to differences in, for example, available spectral bands, spatial information, and calibration quality (e.g., Kahn et al., 2011; Li et al., 2009; Sayer, Munchak, et al., 2014), as well as the inherent limitations in information content available from passive single-view imagers compared to more advanced sensor types (e.g., Hasekamp & Landgraf, 2007).

The National Oceanic and Atmospheric Administration (NOAA) generate a number of S-NPP data products in near-real time to support their operational needs, including aerosol optical depth (AOD, often denoted τ) over oceans and dark land surfaces from VIIRS (Jackson et al., 2013). However, these products, while drawing on EOS-era expertise and producing AOD data with similar quality (Huang et al., 2016; Liu et al., 2014), use different algorithms (hence have different contextual biases) and operate in forward processing mode only. Thus, as algorithm or calibration updates are made, discontinuities arise in the data records as data are not reprocessed retrospectively to provide a self-consistent time series. Additionally, there is no equivalent to the NASA Deep Blue (DB) AOD retrieval algorithm providing coverage over deserts (Hsu et al., 2004) in the NOAA VIIRS data products at the present time. Thus, EOS-era NASA data records are being extended through adaptation for VIIRS, as the older sensors are well past their design lives. By applying similar algorithms to EOS-era and newer sensors, with periodic reprocessing as algorithm and calibration improvements become available, the goal is to provide continuity from the EOS to JPSS eras and facilitate the creation of long-term multisensor climate data records.

The DB algorithm was developed initially (Hsu et al., 2004) to fill in data gaps over bright land surfaces (e.g., deserts) in the Dark Target (DT) AOD algorithm. These gaps are important because deserts are important sources of aerosols such as wind-blown mineral dust (e.g., Ginoux et al., 2010; Koren et al., 2006). DB was included in routine MODIS data processing beginning in Collection 5 (C5); in the following MODIS Collection 6 (C6) and for the present Collection 6.1 (C6.1), the DB algorithm was expanded to include darker (vegetated) land surfaces as well as bright ones (Hsu et al., 2013), and retrieved AOD also becomes more accurate and precise, and its error characteristics are more well quantified (Sayer et al., 2013; Sayer, Hsu, Bettenhausen, Jeong, et al., 2015). This enhanced DB algorithm was also applied to the SeaWiFS record (Hsu et al., 2013; Sayer, Hsu, Bettenhausen, Jeong, et al., 2012). Additionally, in the SeaWiFS DB data product, a SeaWiFS Ocean Aerosol Retrieval (SOAR) algorithm was developed as a complement to the DB over-land data (Sayer, Hsu, Bettenhausen, Ahmad, et al., 2012). Note that SOAR and DB are separate, distinct algorithms. MODIS already had a separate over-water algorithm (Levy et al., 2013; Tanré et al., 1997) distinct from both the DB and Dark Target (DT) land algorithms, developed by a separate algorithm team from SOAR, and so SOAR was not applied to MODIS in C6 or C6.1.

The latest C6.1 DB over-land algorithms have been adapted to work on VIIRS, and to complement them, SOAR has also been extended to take advantage of VIIRS' capabilities and other advances since the SeaWiFS application. DB and SOAR were also recently applied to AVHRR measurements, incorporating some of these updates (Hsu et al., 2017; Sayer, Hsu, Lee, et al., 2017). Because of this, the acronym SOAR is now taken more generically as "Satellite Ocean Aerosol Retrieval." SOAR and DB for VIIRS will together be processed routinely by the NASA Atmospheres Science Investigator-Led Processing System (SIPS) at the University of Wisconsin and be made available freely at the NASA Level 1 and Atmosphere Archive and Distribution System (<https://ladsweb.nascom.nasa.gov>) as the "VIIRS Deep Blue" data set. Further information is also available at the Deep Blue project Web page, <https://deepblue.gsfc.nasa.gov>.

This study describes the adaptation of SOAR for application to VIIRS measurements as provided in Version 1 of the VIIRS Deep Blue data product, expected to be released by the end of 2017, and presents some initial validation. As future algorithm or calibration versions become available, the whole VIIRS mission will be reprocessed periodically to ensure that the data remain self-consistent through time. Section 2 describes relevant characteristics of the VIIRS instrument and its similarities and differences from EOS sensors. Section 3 provides a summary of the SOAR algorithm with a focus on differences from the SeaWiFS application. In section 4 a preliminary validation of the algorithm against Maritime Aerosol Network (MAN) observations is provided, as well as a self-consistency analysis using data from consecutive overlapping VIIRS orbits and comparison against NOAA VIIRS AOD. A fuller validation against Aerosol Robotic Network (AERONET) coastal/island sites, and comparison to other satellite AOD products, will be presented in a forthcoming study. Finally, section 5 provides a summary and details expected further developments.

Table 1
VIIRS Moderate-Resolution (M) Band Central Wavelengths and Centers of Similar MODIS/SeaWiFS Bands

VIIRS name	VIIRS (μm)	SeaWiFS (μm)	MODIS (μm)
M01	0.412	0.413	0.412
M02	0.445	0.444	0.442
M03	0.488	0.491	0.466, 0.488 ^a
M04	0.555	0.555	0.554
M05	0.672	0.668	0.645, 0.666 ^a
M06	0.746 ^a	0.765	0.747 ^a
M07	0.865	0.866	0.867
M08	1.240	-	1.242
M09	1.378	-	1.370
M10	1.61	-	1.64
M11	2.25	-	2.13
M12	3.7	-	3.75
M13	4.05	-	4.05
M14	8.55	-	8.55
M15	10.76	-	11.03
M16	12.01	-	12.02

^aThese bands can saturate at radiances corresponding to land/cloudy scenes, so are not commonly used for atmospheric applications.

2. Relevant Features of the VIIRS Sensor

Like AVHRR, MODIS, and SeaWiFS (among others), VIIRS is a multispectral passive broad-swath single-viewing spaceborne imaging radiometer. It records data in 22 moderate-resolution bands (M-bands) across the visible and thermal infrared spectral regions with a nominal pixel size of 750 m at the center of the swath; the bands are similar to those on MODIS and/or SeaWiFS (Table 1). Note, however, that some of the MODIS bands designed for ocean color applications saturate at radiances found over land or cloudy scenes; the SeaWiFS and VIIRS bands do not saturate in most cases (aside from very strong Sun glint).

The instrument additionally has five imagery-resolution bands (I-bands) with a nominal pixel size of 375 m and band centers close to some M-band positions, and a Day-Night Band (DNB), which is a greatly enhanced follow-on to the previous DMSP Operational Line Scanner sensor for imaging the Earth with high sensitivity during both day and night (Lee et al., 2006). Neither the I-bands nor DNB are used in the present DB or SOAR algorithms so will not be discussed further.

VIIRS has an across-track scanning pattern, similar to MODIS, with 16 M-band detectors per scan. VIIRS incorporates several design features (Wolfe et al., 2013) to reduce the nadir-to-scan edge pixel distortion and overlap, which is an issue for MODIS, commonly referred to as the “bowtie” effect (Wolfe et al., 2012). Essentially, with MODIS, as the detector scans across-track pixels become broader and elongated, and pixels from consecutive scans overlap, which has consequences for retrieval characteristics as a function of scan angle, and can affect aggregated statistics (Sayer, Hsu, & Bettenhausen, 2015). With VIIRS, the native pixel size is actually smaller than the nominal M-band size in the across-track direction. The scan is divided into three regions (in both directions). From nadir out to a scan angle of 31.72°, three pixels are aggregated across track; from 31.72° to 44.86° two pixels are aggregated, and from 44.86° to the edge of scan (56.28°, corresponding to a view zenith angle around 75°) no aggregation is performed. This limits across-track distortion at the end of each aggregation zone to a factor of 2, compared to a factor of about 6 without this oversampling and aggregation. Additionally, at the outer two aggregation zones, two and four pixels, respectively, are deleted from the edge of scan (so-called “bowtie deletion”) to decrease the degree to which consecutive scans overlap.

S-NPP is in a Sun-synchronous orbit at an average altitude of 839 km; the daytime equatorial local solar cross-time at center of swath is around 13:30 UTC (similar to Aqua, although they are on different orbital tracks).

This orbit and the sensor characteristics mean that VIIRS has a swath width of 3,040 km (about 50% broader than MODIS and twice that of SeaWiFS' Global Area Coverage mode), sufficient to remove gaps between consecutive orbits, meaning that the whole sunlit portion of the globe is viewed at least once per day and often twice at midlatitude or high latitude.

VIIRS has similar onboard calibration capabilities to MODIS, and Level 1b (L1b; calibrated reflectance data) requirements are 2% in reflectance (for a reference typical scene brightness) and 2.5%–3% (dependent on band) polarization sensitivity for solar bands. The NASA DB/SOAR data products use NASA L1b as a basis (as opposed to NOAA L1b; the two are slightly different) from the current NASA version 2 L1bs. Further, SOAR processing applies additional absolute calibration corrections from Sayer, Hsu, Bettenhausen, et al. (2017), based on a cross calibration of VIIRS against MODIS Aqua, which were also found to result in improvements to AOD validation statistics against AERONET. Note, however, that these corrections relate only to the absolute radiometric gain of the bands—the trending of the radiometric calibration since launch, monitored using the onboard solar diffuser stability monitor and periodic lunar observations, is well characterized as part of the standard NASA L1b product (Lei & Xiong, 2017; Xiong et al., 2016).

3. Adaptation of SOAR to VIIRS

3.1. Overview

The SOAR algorithm as applied to SeaWiFS was described in detail, and validated, by Sayer, Hsu, Bettenhausen, Ahmad, et al. (2012). The underlying principles of the application to VIIRS are the same, although VIIRS offers several advantages compared to SeaWiFS (chiefly, improved spatial and spectral coverage). Thus, an overview of SOAR as applied to VIIRS in the version 1 data set is provided here, summarized in Figure 1. The algorithm proceeds through several steps:

1. First, suitable sensor pixels for the retrieval are identified. In this context, the term “sensor pixel” refers to the set of spectral VIIRS M-band top of atmosphere (TOA) L1b reflectance or brightness temperature measurements at nominal 750 m spatial resolution, for the same point on the Earth's surface. Here the reflectance ρ_i for band i is defined as the TOA measured radiance L integrated across the sensor spectral response function Φ_i for that band, divided by the solar spectral irradiance E_0 (corrected for Earth-Sun distance) integrated across the band; that is,

$$\rho_i = \frac{\int_0^\infty L(\lambda)\Phi_i(\lambda)d\lambda}{\int_0^\infty E_0(\lambda)\Phi_i(\lambda)d\lambda}, \quad (1)$$

where λ denotes wavelength. Note that some algorithms define reflectance different by a factor of π/μ_0 from this (where μ_0 is the cosine of the solar zenith angle).

2. An inversion procedure is used to estimate aerosol properties from the measured spectral reflectance: specifically, AOD at the reference wavelength of 550 nm (references to AOD not mentioning wavelength should be taken to mean 550 nm) and the fine-mode fractional contribution to AOD at 550 nm (FMF), under the assumption of a bimodal aerosol distribution. Note that the SeaWiFS application of SOAR reported fine-mode fraction of aerosol volume rather than of AOD; the change to FMF of AOD reflects both the fact that discussions with data users suggested that this parameter would be more useful and also an easier interface with radiative transfer codes. The AOD at 550 nm is considered the primary data product.
3. These pixel-level retrievals are aggregated along track and across track in groups of 8×8 contiguous pixels (6×6 km horizontal pixel size), known as “cells” or “retrieval pixels” (as distinct from sensor pixels). Quality assurance (QA) tests are performed to estimate the confidence in these cell-aggregated values and assign each cell a QA value. These aggregated retrievals and associated diagnostic information, together with over-land retrievals from the DB algorithm, constitute the Level 2 (L2, orbit-level) data product.

As well as these two main retrieval outputs, the AOD and FMF are used with the retrieved aerosol optical model to determine the spectral AOD at each VIIRS band used, as well as the Ångström exponent (denoted AE or α). The AE is the negative of the gradient of AOD with respect to wavelength (both in log space), typically evaluated across a pair of wavelengths λ_1, λ_2 as

$$\alpha = -\frac{d \log(\tau(\lambda))}{d \log(\lambda)} \approx -\frac{\log \frac{\tau_{\lambda_1}}{\tau_{\lambda_2}}}{\log \frac{\lambda_1}{\lambda_2}}. \quad (2)$$

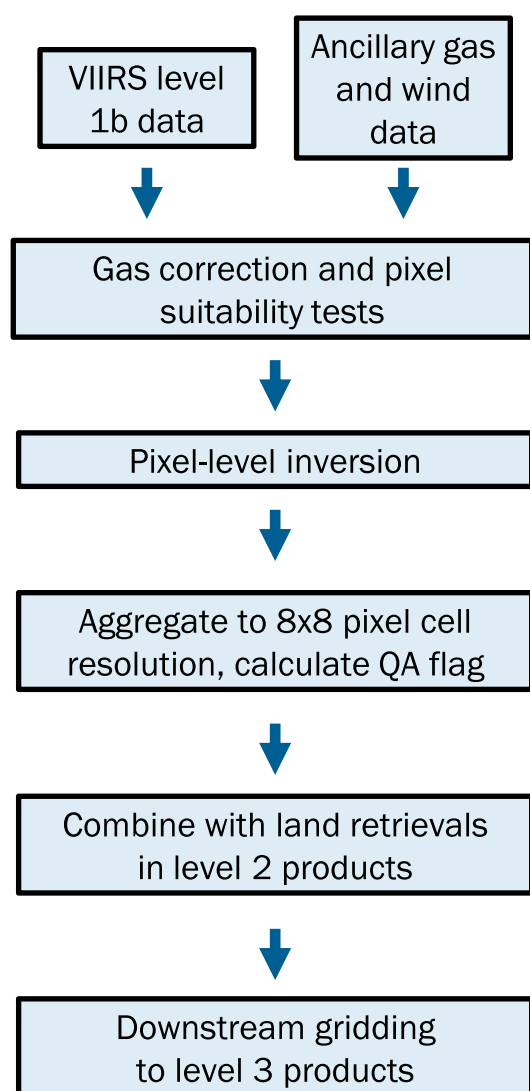


Figure 1. Chart summarizing SOAR algorithm flow, as applied in the NASA VIIRS “Deep Blue” version 1 data set.

For the VIIRS application of SOAR, the AE is calculated over the wavelength range 550–870 nm.

Temporal gridded composites (e.g., daily and monthly) of L2 data at 1° are also created and known as Level 3 (L3) products. L2 data are often most useful for investigation of individual case studies or when a high-resolution look at a scene is required, while L3 data are often most useful for multisensor, or satellite to model, data comparisons and climatological studies.

In addition to the VIIRS data, SOAR makes use of ancillary fields of meteorological data from the NASA Goddard Earth Observing System Model, Version 5 (GEOS-5) Forward Processing for Instrument Teams (FP-IT) data stream, available from <http://gmao.gsfc.nasa.gov/products>. These are obtained at 3-hourly temporal and 0.5° latitude/0.625° longitude resolution and interpolated (linearly in space and time) to each VIIRS sensor pixel. The parameters used are the near-surface wind speed, total column ozone amount, and total column water vapor amount.

3.2. Sensor Pixel Selection

SOAR is applied to all daytime (defined as solar zenith angle <84°) sensor pixels determined to be over water (whether sea/oceanic or inland water) and not obstructed by clouds, snow, or ice or strong Sun glint. The VIIRS internal land/sea mask is used to determine whether a pixel is classified as water or not. The presence or possibility of contamination by clouds, snow, or ice is determined by the following tests; pixels failing these tests are discarded. Bowtie-deletion pixels are treated as missing data for purposes of the tests below (e.g., not used for computation of spatial variability). Note that gaseous transmittance corrections are performed on the data at this stage, using the ingested meteorological data (more detail is provided by Sayer, Hsu, Bettenhausen, et al., 2017).

3.2.1. Cloud Mask

If a pixel fails any of the following tests, it is marked as cloudy and discarded. Thresholds have been determined empirically based on manual inspection of cloudy and clear scenes, although the principles behind these tests have a long heritage in aerosol remote sensing applications (e.g., Hsu et al., 2013, Martins et al., 2002, Sayer, Hsu, Bettenhausen, Ahmad, et al., 2012).

Spatial variability. This test is based on the principle that clouds typically show small-scale heterogeneity to a greater extent than aerosols or the

ocean surface. The 3 × 3 pixel moving windows (from which land pixels are excluded) are used to calculate the standard deviation of reflectance in bands M01 (412 nm) and M08 (1,240 nm). If either is above a threshold value of 0.0025 μ_0 , then the pixel is marked as cloudy. At latitudes poleward of 65°N the M08 threshold is strengthened to 0.001 μ_0 ; otherwise detection of low, homogeneous Arctic fog was found to be unreliable.

High cloud test. This test is based on the principle that signals in band M09 (1,375 nm) over ocean are likely to originate from high altitudes (at which the presence of aerosols is unlikely), due to strong water absorption in this band in the lower troposphere. If the reflectance in band M09 is over 0.004 μ_0 then the pixel is marked as cloudy.

Absolute brightness. This test is based on the principle that clouds are bright, while extreme brightness at blue wavelengths is unlikely for aerosols because aerosols likely to have a high AOD also tend to absorb light at blue wavelengths. Thus, if the reflectance in band M03 (488 nm) is over 0.11 μ_0 , then the pixel is marked as cloudy.

Cloud adjacency. This test is based on the principle that pixels near to clouds may contain undetected clouds or cloud fragments or be subjected to other issues (e.g., 3-D effects; Várnai & Marshak, 2009), which are not captured by the radiative transfer model. A 3 × 3 pixel area centered on each pixel identified as cloudy

(i.e., extending 1 pixel out in each direction along track and across track) is discarded as potentially contaminated. Note that this test only checks for pixels flagged as cloudy by the above over-ocean checks and is only applied to over-ocean pixels (i.e., does not influence, and is not influenced by, land pixels or bowtie-deletion pixels).

Additional postretrieval quality checks (discussed later) are used to identify retrievals which may suffer from residual cloud contamination.

3.2.2. Sun Glint Mask

The Sun glint strength is estimated for each pixel using the ingested near-surface wind speed and the isotropic-wind model of Cox and Munk (1954a, 1954b). If the estimated glint reflectance is over 0.005, then the pixel is discarded, as uncertainties in the surface reflectance model (related to wind speed/direction) may overwhelm the aerosol signal.

3.2.3. Turbid/Shallow Water Mask and Algorithm Switch

Pixels are also assessed to determine whether they are likely contaminated by turbid or shallow waters. These waters appear brighter in the midvisible than the assumed open-ocean ("Case 1") model (Morel & Prieur, 1977), and as a result lead to (normally positive) biases in retrieved AOD if not identified and removed. However, shortwave infrared (swIR) wavelengths are affected negligibly in most cases. Thus, a two-part turbid/shallow water detection scheme is applied to each cloud-free sensor pixel.

The first part is based on the algorithm of Li et al. (2003), which has been used widely for MODIS, SeaWiFS, and VIIRS measurements, and is robust to the presence of aerosols. Essentially, it performs a power law fit of measured reflectance versus wavelength in the blue and swIR bands; the presence of turbid or shallow water is diagnosed if the M04 (555 nm) TOA reflectance exceeds a positive threshold deviation (Δ_{555}) from this power law. Three regimes are identified in the present application:

$\Delta_{555} < 0.015\mu_0/\pi$. No turbid or shallow water is detected, and the retrieval is performed using the seven VIIRS bands centered near 488, 555, 672, 865, 1240, 1610, and 2250 nm. This is known as the "full" retrieval.

$0.015\mu_0/\pi < \Delta_{555} < 0.1\mu_0/\pi$. Moderate turbid or shallow water is detected. In this case only the nIR and three swIR bands (865, 1,240, 1,610, and 2,250 nm) are used in a "backup" retrieval, although the algorithm otherwise proceeds normally. Note that this differs from previous applications of this type of mask, which tend to simply discard such contaminated pixels (e.g., Levy et al., 2013; Sayer, Hsu, Bettenhausen, Ahmad, et al., 2012). A flag is provided in the L2 products to indicate whether the retrieval pixel value is taken from a sensor pixel that was identified as moderately turbid/shallow or not. Due to the lower information content, this four-band retrieval is expected to perform more poorly than the seven-band retrieval, although it does permit coverage where pixels would otherwise be discarded. Further evaluation will guide usage recommendations for pixels so affected.

$\Delta_{555} > 0.1\mu_0/\pi$. Severe turbid/shallow water is detected. In this case there can be some residual surface contaminant contributing a nonnegligible signal in the nIR/swIR bands, and so the pixel is flagged as unsuitable for processing.

The second part of the detection scheme is to filter out areas of permanent shallow or turbid water using ancillary data sets, in case of occasional failure of the above spectral test. Pixels are defined as shallow water if the depth from the elevation and topography at 1 arc min (ETOPO1) bathymetry data set (Amante & Eakins, 2009) is less than 20 m. At this depth at a wavelength of 550 nm, for pure water with a white (albedo equal to 1) sea bottom being viewed from directly above, approximately 85% of the light penetrating the sea surface would be absorbed (slightly less for shorter wavelengths, significantly more for nIR/swIR wavelengths; Sayer, Thomas, & Grainger, 2010). For real seawater with absorbing impurities and a nonwhite seafloor, the fraction of light absorbed would be higher, and thus, any light reflected off the sea bottom and reaching the satellite can be considered negligible for water of this depth or greater. Note that ETOPO1 provides elevation or bathymetry relative to sea level, so inland waters in elevated locations may register as shallow even if deeper than 20 m in some cases.

To define permanently turbid water, a gap-filled climatology (one value for each of the 12 calendar months at 0.1° resolution, cf. Sayer, Hsu, Bettenhausen, et al., 2017) of SeaWiFS-derived chlorophyll (Chl) concentration (Hu et al., 2012) is used. Pixels with climatological Chl $> 3 \text{ mg m}^{-3}$ are denoted permanently turbid.

If the test on Δ_{555} indicates clear water but either the bathymetry or Chl tests are failed, the retrieval also proceeds with the four-band backup retrieval. These threshold values are all somewhat subjective, although

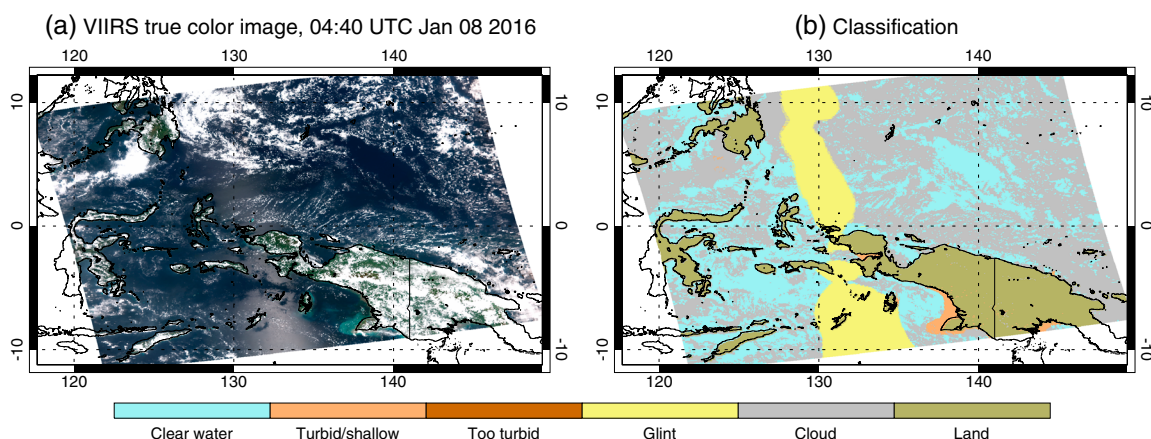


Figure 2. Example (a) true-color image and (b) SOAR pixel classification map.

reasonable based on manual examination of scenes and physical intuition, and small variations do not significantly affect the classifications determined by these tests.

3.2.4. Example of Pixel Suitability Tests

An example of pixel classification from these tests is given in Figure 2. Note that the slightly jagged appearance of the Sun glint exclusion zone is due to the sensor scan pattern, which results in small discontinuities in view azimuth angle, and so glint strength, between adjacent (16 pixel) scans. Note also that, for this example, no pixels fall into the “too turbid/shallow” category.

3.3. Pixel-Level Retrieval

Look-up tables (LUTs) of TOA reflectance for a variety of atmospheric and surface conditions are required to transform between measurement space (reflectance) and state space (AOD and FMF), as accurate radiative transfer calculations are currently too slow to perform on the fly. These LUTs are generated using the vector linearized discrete ordinates (VLIDORT) radiative transfer model (Spurr, 2006). VLIDORT is a vector radiative transfer code, able to handle nonspherical aerosol models, pseudospherical atmospheres, and a bidirectional reflectance distribution function (BRDF) description of surface reflectance. The LUTs are generated for each of 22 solar zenith, 20 view (sensor) zenith, and 21 relative azimuth angles, spaced regularly, 6 wind speeds (1, 3, 6, 9, 12, and 15 ms^{-1}), and 4 values of Chl (0.01, 0.1, 1, and 10 mg m^{-3}).

3.3.1. Aerosol Optical Models

LUTs are generated for each of four distinct aerosol models, with AOD/FMF node points (dictating state space bounds) given in Table 2. Ranges were based on physically reasonable values, with node points to ensure that linear interpolation between them results in $<1\%$ error in most cases compared to exact state calculations (i.e., smaller than calibration uncertainty). All models consist of bimodal lognormal distributions (with smaller and larger modes referred to as “fine” and “coarse,” respectively). For an individual (fine or coarse) aerosol mode, the particle volume concentration $V(r)$ is calculated as follows, where r denotes particle radius, C_v the total particle volume (proportional to aerosol mass and AOD, for a given size), r_v the modal volume radius, and σ the geometric standard deviation:

$$\frac{dV(r)}{d \ln(r)} = \frac{C_v}{\sqrt{2\pi}\sigma} e^{-\frac{1}{2} \left(\frac{\ln(r) - \ln(r_v)}{\sigma} \right)^2}. \quad (3)$$

Values of the parameters r_v , σ for each model are provided within the references given in Table 2. The “maritime” model is designed to represent background marine conditions, for example, sea spray aerosol with limited influence from other types (O’Dowd & de Leeuw, 2007). The “dust” model represents aeolian dust, and “fine-dominated” model represents aerosols with a significant contribution from, for example, smoke or industrial emissions. Although smoke and industrial aerosols can have highly variable optical properties dependent on source and aging effects (e.g., Wang & Martin, 2007; Sayer, Hsu, et al., 2014), at present only a single model is used, as a follow-on from the SeaWiFS and AVHRR applications. Finally, a “mixed” model uses the fine mode from the fine-dominated model, and the coarse mode from the dust model, to represent elevated-AOD cases where both fine and coarse aerosols contribute significantly to the aerosol burden (such as mixed smoke and dust as can be found in the Sahel, or near the edges of plumes where smoke or dust mix into the background).

Table 2

Aerosol Optical Model References and LUT Node Points Used in the SOAR-VIIRS Version 1 Data Set

Model name	Reference	LUT node points
Mineral dust	Lee et al. (2017)	AOD: 0.15, 0.25, 0.4, 0.6, 0.8, 1, 1.25, 1.5, 2, 2.5, 3, 3.5, 4, 5 FMF: 0, 0.1, 0.2, 0.3, 0.4
Fine dominated	Sayer, Hsu, Bettenhausen, Ahmad, et al. (2012)	AOD: 0.2, 0.3, 0.4, 0.6, 0.8, 1, 1.25, 1.5, 2, 2.5, 3, 3.5, 4, 5 FMF: 0.7, 0.75, 0.8, 0.85, 0.9, 0.95, 1
Maritime	Sayer, Smirnov, Hsu & Holben (2012)	AOD: 0.001, 0.04, 0.08, 0.12, 0.16, 0.2, 0.25 FMF: 0.1, 0.2, 0.3, 0.4, 0.5, 0.6, 0.7, 0.8
Mixed	Sayer, Hsu, Bettenhausen, Ahmad, et al. (2012) and Lee et al. (2017)	AOD: 0.2, 0.3, 0.4, 0.6, 0.8, 1, 1.25, 1.5, 2, 2.5, 3, 3.5, 4, 5 FMF: 0.4, 0.5, 0.6, 0.7

In future data versions the use of additional or alternative optical models will be examined. Aerosol vertical profiles are assumed to be homogeneous layers from 0 to 1 km (marine), 0 to 2 km (fine-dominant, mixed), or 1 to 3 km (dust), although the sensitivity of the bands used to aerosol vertical distribution within realistic ranges is in most cases minor (<3% in reflectance).

These optical models are essentially the same as in the SeaWiFS application of Sayer, Hsu, Bettenhausen, Ahmad, et al., (2012), except that the spherical dust model has been replaced with a nonspherical one (also used for the coarse mode of the mixed aerosol model), which reduces AOD/FMF retrieval error by better accounting for the angular distribution of scattered reflectance (Lee et al., 2017, 2012; Mishchenko et al., 1997). A full description of this dust model and illustration of the effect of the sphericity assumption is provided by the companion paper, Lee et al. (2017). Additionally, SeaWiFS covered the spectral range 412–865 nm; for VIIRS bands outside this range (M08, M10, and M11) real and imaginary aerosol refractive indices have been decreased based on spectral dependency of refractive index from Hess et al. (1998), as there are few measurements of aerosol optical properties across the whole VIIRS spectral range. The range of spectral dependence of AOD, single scattering albedo (SSA), and asymmetry parameter (ASY) covered by these models (for their minimum and maximum FMF node points, Table 2) are shown in Figure 3.

Although aerosol type is a retrieved quantity via the best fit optical model (see section 3.4), it is important to emphasize that these model names are interpretive types (for ease of descriptiveness) only. The satellite and retrieval algorithm do not know and cannot make any direct judgment about the origin or specific chemical composition of an aerosol-laden air mass. Although it is an easy shorthand to refer to, for example,

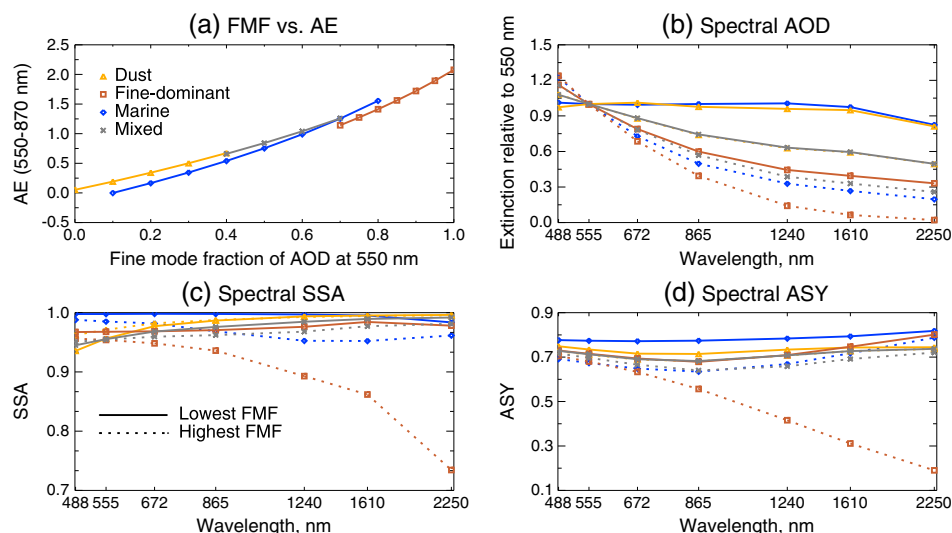


Figure 3. Properties of aerosol optical models used in the SOAR VIIRS version 1 algorithm. (a) The relationship between FMF and AE and (b–d) the range of spectral dependence of AOD, SSA, and ASY, respectively, for each aerosol model: dust in orange, fine dominated in brown, maritime in blue, and mixed in gray. Properties for lowest and highest FMF are shown with solid and dotted lines, respectively.

a “dust aerosol model,” when such a model is chosen as the retrieval solution, it is more correct to say that the satellite measurements may be best fit with an optical model whose properties (size/shape distribution and spectral complex refractive index) are consistent with optical properties often associated with mineral dust aerosols, as opposed to saying definitively that the observation is one of a dust-laden air mass. The measurements are optical ones, and thus, it is the optical outputs (i.e., AOD and its spectral dependence), which are most directly constrained by them.

3.3.2. Improved Surface Reflectance Model

The ocean surface BRDF is an updated version of the treatment used by Sayer, Hsu, Bettenhausen, Ahmad, et al. (2012) for SeaWiFS. In brief, the BRDF model draws on the widely used method of Koepke (1984) and includes contributions from oceanic whitecaps, Sun glint, and scattering from within the water (“underlight,” using the basic formalism of Austin, 1974). Both the whitecap and underlight terms have been updated since the SeaWiFS application, largely to extend the spectral range of applicability and update older parametrizations and coefficients with more recent data. Specific details of the updates are provided in Sayer, Hsu, Bettenhausen, et al. (2017) and are omitted here for brevity.

3.3.3. Minimization Procedure

The retrieval solution is found by comparing the difference between reflectance values stored in the LUTs and the TOA measurements (the “residuals”) and minimizing the sum of square residuals across all bands, to simultaneously determine the AOD and FMF most consistent with the measurements. The minimization is iterative, and the first guess is taken as the LUT node point with the minimum sum of square residuals. Minimization uses the method of Levenberg (1944) and Marquardt (1963) and is performed with AOD and FMF as free parameters, that is, retrieval of two parameters from seven (or four, in the case of turbid/shallow water) measurements. LUTs are interpolated linearly in the minimization. Wind speeds out of bounds (<1 or $>15 \text{ ms}^{-1}$) are set to the minimum/maximum in the LUT, as appropriate. The Chl climatology interpolation similarly truncates out-of-bounds values; note that the Chl dimension of the LUT is interpolated in $\log_{10}(\text{Chl})$ since underlight varies approximately linearly with the logarithm of Chl. In both cases, this truncation has a negligible influence on retrieval performance.

The sum of square residuals at the solution is normalized by the number of degrees of freedom (i.e., five for the full open-water algorithm or two for the backup turbid/shallow water algorithm). This is referred to hereafter as the χ^2 statistic, sometimes also called retrieval cost; that is,

$$\chi^2 = \frac{1}{n_m - n_{\text{ret}}} \sum_{i=1}^{n_m} \left(\frac{\rho_{\text{LUT},i} - \rho_{\text{m},i}}{\sigma_i} \right)^2, \quad (4)$$

where n_m indicates the number of bands used (seven or four), n_{ret} indicates the number of retrieved quantities (two), and $\rho_{\text{LUT},i}$, $\rho_{\text{m},i}$, and σ_i the modeled reflectance from the LUT, measured reflectance, and assumed uncertainty on band i , respectively. A relative uncertainty of 4% (bands M05 and M07), 5% (M03, M04, and M08), 6% (M10), or 7% (M11) on the measurements is assumed (reflecting calibration and forward model uncertainty and including uncertainty in ancillary trace gas data), with a floor of 10^{-5} in reflectance units (to avoid numerical issues). Note that the formulation of equation (4) implicitly assumes that these uncertainties are uncorrelated spectrally. When the reduced four-band nIR/swIR retrieval is performed for pixels identified as turbid (section 3.2.3), the uncertainty on band M07 (865 nm) is increased to 8% to account for the possibility of a residual turbidity contribution in this band. These values may be refined in the future. If the measurements are consistent with the retrieved state given the assumed uncertainties in the measurements and forward model, then the retrieval should have a χ^2 statistic around 1. More generally, the (nonnormalized) sum of square residuals over an ensemble of retrievals should follow a χ^2 distribution with degrees of freedom equal to the number of degrees of freedom in the retrieval.

The minimization is performed for each of the candidate aerosol optical models in succession, which is in contrast to the SeaWiFS application, in which the AOD/FMF space was contained within a single LUT (with different aerosol optical properties in different sections of the LUT). This helps to avoid numerical instabilities near discontinuities and allows for overlapping AOD/FMF combinations between different aerosol model LUTs.

The MODIS Dark Target ocean and NOAA VIIRS ocean retrievals compute LUTs for the fine-mode and coarse-mode aerosol contributions to TOA reflectance separately and then weight these by FMF on the fly during their retrieval procedure, using the linear mixing approximation to compute the total reflectance

(Tanré et al., 1997). That approach has the advantage of being computationally inexpensive, but the linear mixing approximation introduces systematic errors in the modeled reflectance when there is absorption in the atmospheric column, which leads to biases in retrievals (e.g., Abdou et al., 1997). In contrast, the radiative transfer in the SOAR LUTs combines both the fine-mode and coarse-mode aerosols self-consistently, increasing the computational cost but avoiding the linear mixing approximation and the biases that introduces.

3.4. Aggregation to Level 2 (Cell) Resolution and Quality Assurance

After each sensor pixel has been processed with each aerosol model, the sensor pixel retrievals are aggregated to 8×8 sensor pixel (nominal 6×6 km) resolution, referred to as L2 “retrievals” or cells. In principle, the data could be aggregated to a finer resolution than 8×8 sensor pixels, and this could be done in the future if there is user demand. For the initial version 8×8 pixels was chosen as this corresponds to half a VIIRS M-band scan and matches the NOAA product. Going to a finer resolution may improve the utility of the data for some applications but risks an increase in error due to factors such as 3-D effects, pixel or band misregistration, and susceptibility to radiometric or algorithm noise (e.g., Remer et al., 2013).

For this aggregation, the cell median values from all processed pixels within the cell are reported, which decreases sensitivity to outliers (from e.g., undiagnosed cloud contamination). This is in contrast to the SeaWiFS application, for which cell means were calculated. This step is performed for each candidate aerosol model, and then the results for the model with the lowest χ^2 are reported in the L2 product. In this way, an interpretive aerosol type (section 3.3.1) corresponding to this best fit aerosol optical model is also provided. Note that there are no geographical constraints on aerosol model selection.

A QA value is then assigned. If at least 30% of the (non-bowtie-deleted) pixels in the 8×8 cell had a retrieval performed, the value of χ^2 is under 10, the AOD is less than 4.95 (i.e., the retrieval does not hit the upper limit for the dust model, which could be indicative of cloud), and the AOD standard deviation within the cell is less than 0.5, then the cell is assigned QA = 3 (referred to as “high quality” or “high confidence”). Otherwise, the cell is deemed to be of low quality and assigned QA = 1. The 30% data volume test (largely related to proximity to clouds) tends to be the most common reason for assignment of QA = 1, leading to about two thirds of pixels being assigned QA = 1; most of the remainder result from the χ^2 threshold. For the four-band “turbid” retrieval path, the data volume threshold is increased to 50% as affected retrievals tend to be near coastlines, and a stricter threshold was found to be effective at removing pixels, which could be on land/water boundaries (i.e., mixed surface cover) as well as those most likely to be affected by adjacency effects. With these thresholds, approximately 80% of populated cells are assigned QA = 3 globally. Small changes to these thresholds were found empirically to affect the data volume but not significantly affect the statistics of the population of retrievals, or the level of agreement with validation data.

The QA flag range 1–3 is used for continuity with EOS-era heritage data products, although in this case it is a binary classification (1 or 3 corresponding to “bad” and “good,” respectively; no QA = 2). This binary classification was adopted to reduce user confusion about which retrievals should be considered for scientific applications, and also because, after testing various ways that retrieval quality could be assessed during the development of the data set, no significant intermediate cluster of retrievals that would merit being called QA = 2 was identified.

An example granule from 1 September 2013 illustrating these two main direct retrieval outputs (AOD and FMF) after QA filtering is shown in Figure 4. This shows a “river of smoke” flowing from southern Africa into the southern Indian Ocean, which is a common feature of the aerosol system in this part of the world around this time of year (e.g., Swap et al., 2003, and references therein). The contrast between this transported smoke plume and the background, more pristine, ocean is evident in both retrieved quantities.

3.5. Algorithmic Uncertainty Discussion

As a result of the extensive development and application of the numerous DMSP and EOS-era sensors and AOD retrieval algorithms to which VIIRS and SOAR owe their heritage, the various factors influencing retrieval performance and strengths and limitations of this type of sensor and algorithm are fairly well understood (e.g., Levy et al., 2013; Mishchenko et al., 1999; Sayer, Hsu, Bettenhausen, Ahmad, et al., 2012; Sayer, Thomas & Grainger, 2010; Tanré et al., 1996; Zhang & Reid, 2006). Some key summary information is provided here:

1. A calibration uncertainty of $\sim 3\%$ contributes an AOD uncertainty of order 0.01 for low or moderate aerosol loading, if biases at different wavelengths are not strongly correlated spectrally. If biases are systematic

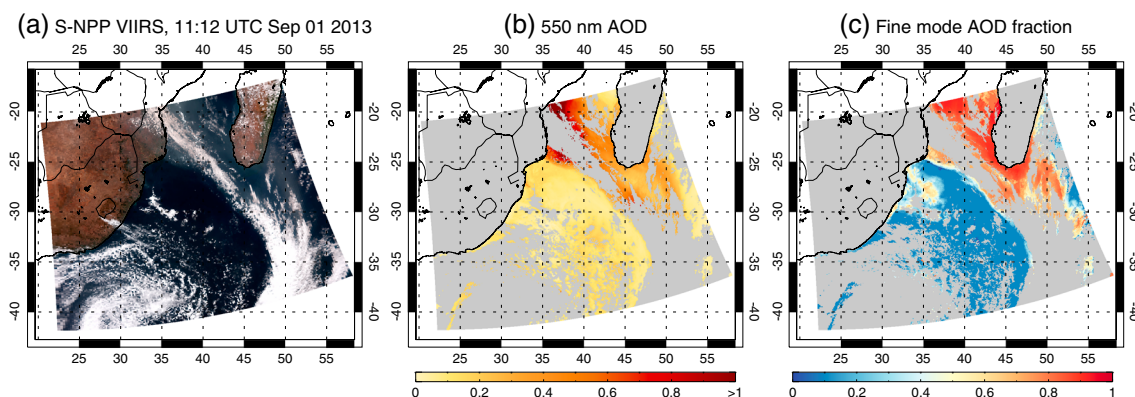


Figure 4. Example retrieval results at L2 resolution. (a) A true-color image, as well as retrieved (b) AOD at 550 nm and (c) FMF. L2 cells without QA = 3 retrievals are shaded in gray.

across different wavelengths, AOD biases are larger and become AOD dependent, dependent on the magnitude and extent of spectral correlation. FMF and α become more strongly affected.

2. Ingesting wind speed data with a random error of $1-2 \text{ ms}^{-1}$ leads to ~ 0.01 AOD uncertainty outside Sun glint regions. In strong Sun glint, wind errors of this magnitude can lead to over 100% relative uncertainty in AOD in some cases, with strong spatial correlation (i.e., systematic biases dependent on the sign of the wind speed error and pixel location relative to glint maximum), which is why pixels under strong glint are excluded. Uncertainties are on average smaller far from the edge of the glint exclusion zone, and larger close to it.
3. The uncertainty on the Chl climatology is unclear, but a $\sim 30\%$ uncertainty in Chl typical for an individual retrieval (Hu et al., 2012) should result in random errors of typically 0.01 in AOD. This is because many of the wavelengths used are affected only weakly by underlight under typical open-ocean conditions, and for bands M03 and M04 (which are more strongly affected) underlight biases are similar in sign and opposite in magnitude so partially cancel out.
4. Uncertainty in aerosol optical model propagates to an AOD-dependent uncertainty in AOD; as VIIRS (like MODIS) has swIR bands, which SeaWiFS lacked, this is likely to be of order 5–10% in AOD (as opposed to 15% for the previous applications to SeaWiFS and AVHRR). The chief contributing factors are the absolute values and spectral behavior of SSA and phase function. The previous SeaWiFS application (as well as the operational MODIS over-water AOD algorithm; Levy et al., 2013) assumes spherical dust, which further increases uncertainties for retrievals in cases of dust particles, although that is addressed for this application to VIIRS and AVHRR through the use of nonspherical models (Lee et al., 2017). VIIRS performance is expected to be superior to that of SeaWiFS and AVHRR, because the swIR bands provide increased sensitivity to aerosol size and so ability to distinguish between fine-dominated and coarse-dominated aerosol mixtures (e.g., Tanré et al., 1996).
5. Numerical artifacts resulting from, for example, LUT interpolation are in most cases small (1% or less in reflectance), that is, smaller than sensor calibration uncertainty, and thus contribute negligible additional retrieval uncertainty.
6. The L2 cell horizontal pixel size (6 km) is somewhat smaller than the typical scale of aerosol horizontal variability (Anderson et al., 2003), which should lead to negligible artificial smoothing of the horizontal aerosol distribution in most cases, especially since oceans are often far from strong aerosol point sources.

As a result of the above factors, the total uncertainty (one standard deviation confidence interval) on retrieved AOD at 550 nm is anticipated to be of order $0.03 + 10\%$. Some preliminary validation is provided later in this manuscript, although further studies will be required to provide a robust quantification and prognostic uncertainty model. The uncertainty on FMF and AE is harder to summarize as it is more situational and much more strongly dependent on the spectral behavior of any sensor calibration bias. Experience with similar sensors and algorithms (Kleidman et al., 2005; Levy et al., 2013; Sayer et al., 2012; Schutgens et al., 2013) suggests a one standard deviation confidence interval of around 0.2 for FMF and 0.4 for AE (better in high-AOD conditions).

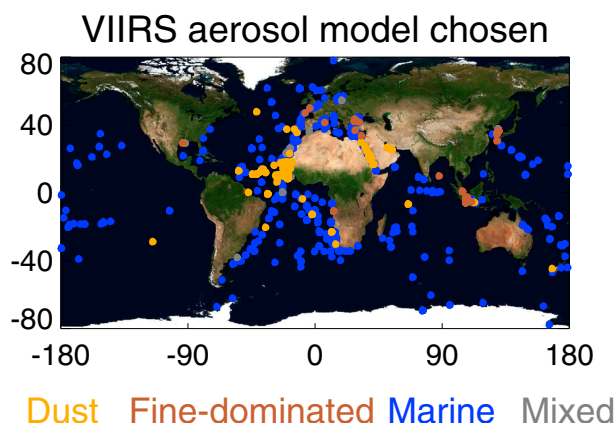


Figure 5. Locations of VIIRS/MAN matchups. Points where the majority of VIIRS retrievals averaged in the matchup selected the dust model are shown in orange, fine dominated in brown, maritime in blue, and mixed in dark gray.

4. Preliminary Validation, Self-Consistency, and Intercomparison Analysis

4.1. Validation Against Shipborne MAN Observations

This section presents an initial validation of the VIIRS SOAR AOD against direct-Sun MAN observations (Smirnov et al., 2011, 2009). These ship-based AOD measurements provide an invaluable resource by providing validation data for AOD retrievals in both coastal areas as well as open oceans, which are otherwise unrepresented in the coastal/island AERONET data. An evaluation against coastal/island AERONET sites will be presented in a follow-up study, along with a comparison of the data against other space-based AOD data sets. The purpose of the present analysis is to provide an indication of the performance of the retrieval over a broad variety of aerosol conditions and geographic regions.

MAN data are collected with hand-held Microtops II Sun photometers, which determine AOD with an accuracy of approximately 0.02 (Knobelspiesse et al., 2004). In this analysis, the “series average” (data acquired with a gap of <2 min between observations) Level 2.0 MAN product (cloud screened and quality assured; Smirnov et al., 2009) is used. The validation protocol is as in Sayer, Hsu, Bettenhausen, Ahmad, et al. (2012). The MAN AOD data are first converted to 550 nm using the closest available MAN wavelength (typically 500 nm) and the MAN Ångström exponent; this interpolation adds negligible additional uncertainty. The median of VIIRS retrievals within a circle of 25 km radius around the ship location at the time of the MAN measurement series is used, to help mitigate the effects of variability in the underlying aerosol field, although sampling and homogeneity issues cannot be solved entirely using this methodology (e.g., Hyer et al., 2011; Kahn et al., 2011).

This protocol yields 836 direct-Sun comparisons; many of these are in the tropical Atlantic and Mediterranean, due to frequent cruises within this region. The locations are shown in Figure 5, and the aerosol optical model chosen by the SOAR algorithm (illustrated in this figure) is qualitatively as expected from prior knowledge about regionally dominant aerosol types. Again, it is important to emphasize that these aerosol optical model names are human-assigned interpretive “types,” based on the assumed dominant aerosol sources of the sites from which AERONET inversion data (i.e., aerosol size/shape distribution and spectral complex refractive index) were used to define these models. The retrieval does not inherently know and cannot directly assess the chemical composition of aerosols sensed. For most type-dependent aerosol analyses, therefore, it is more informative to assess the retrieved quantities more closely tied to the optical constraints of the satellite measurements, that is, AOD, FMF, and AE. It is also important to note that since the number of matchups in any given ocean basin is limited, and they may not cover all seasons, this map should not be taken as a representative map of frequency of occurrence of any particular aerosol type.

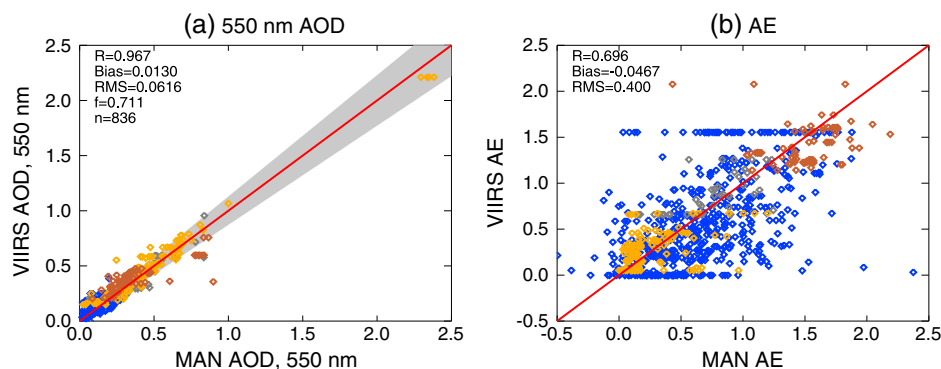


Figure 6. Scatterplots comparing VIIRS and MAN (a) AOD at 550 nm and (b) AE. Comparison statistics are given in each panel. The shaded gray region on the AOD plot indicates $\pm(0.03 + 10\%)$. Points where the majority of VIIRS retrievals selected the dust model are shown in orange, fine dominated in brown, maritime in blue, and mixed in dark gray.

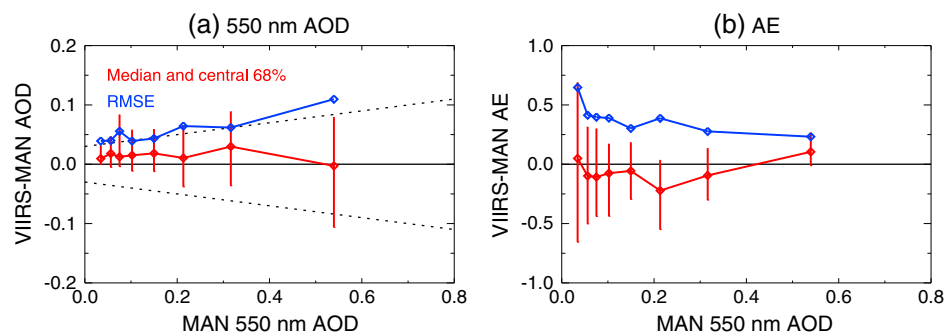


Figure 7. Retrieval error characteristics as a function of MAN AOD at 550 nm for (a) AOD and (b) AE. Red symbols and lines denote bin median and central 68% range of data, respectively. The RMSE for the data in each bin is shown in blue. In Figure 7a, The dashed lines indicate $\pm(0.03 + 10\%)$.

Results of the comparison and summary statistics are shown in Figure 6. For AOD, the correlation coefficient is very high (0.97), although this is driven in part by the small number of MAN points with an AOD around 2.3, which correspond to dust-laden scenes in the tropical Atlantic. Spearman's rank correlation, which is less sensitive to extrema like these, is 0.94, confirming that these outliers do not distort the apparent level of agreement very strongly. The median bias is small and positive (0.013), very close to that found by Sayer, Hsu, Bettenhausen, et al. (2017) for low-AOD scenes at coastal/island AERONET sites using a slightly older algorithm version. Overall, 71.1% of points match the MAN AOD to within the aforementioned confidence envelope $\pm(0.03 + 10\%)$. Expected error (EE) envelopes of this type are intended to provide a one standard deviation confidence interval on the AOD data sets, that is, approximately 68.4% of points should fall within this expected uncertainty, 95% within twice it, following Gaussian statistics. Thus, this comparison suggests that the VIIRS data set meets this target, although this is only a preliminary validation exercise. Figure 7 shows the error characteristics as a function of MAN AOD, split into eight equally populated bins (and reported at the bin-median MAN AOD); this indicates that the data appear approximately compliant with this EE metric across the range of AOD sampled.

A future comprehensive evaluation against AERONET sites will be performed to quantify the level of retrieval error more robustly, examine the contextual (i.e., geometric and AOD/aerosol type dependence) of these errors, and develop retrieval-level uncertainty estimates in the same way as has been done for MODIS Deep Blue data products (Sayer et al., 2013; Sayer, Hsu, Bettenhausen, Jeong, et al., 2015; Sayer, Munchak, et al., 2014). An advantage of AERONET over MAN for the quantification of EE and retrieval biases is the larger data volume and repeat observations at a single location, plus a lower-AOD uncertainty (~ 0.01 for AERONET compared to ~ 0.02 for MAN; e.g., Eck et al., 1999), the downside being that AERONET samples islands/coasts rather than the open ocean. Nevertheless, the results of this MAN comparison suggest that the uncertainty of this new data set is already comparable to EOS-era records from SeaWiFS and MODIS (e.g., Levy et al., 2013; Sayer, Hsu, Bettenhausen, Ahmad, et al., 2012; Sayer, Smirnov, Hsu, et al., 2012).

The retrieved AE (Figure 6b) is also well correlated ($R = 0.70$) with MAN and shows little bias (-0.05) and an RMS error of 0.40. This is somewhat improved upon SeaWiFS performance (Sayer, Hsu, Bettenhausen, Ahmad, et al., 2012), due to a combination of the additional swIR spectral bands on VIIRS and the incorporation of a spheroidal (as opposed to spherical) particle dust optical model. The difference in wavelength range for the AE calculation (500–870 nm for MAN and 550–870 nm for SOAR) should introduce minimal additional disagreement. Figure 7b shows that the AE appears to have small bias across the whole range of AOD sampled, while the error decreases from around 0.5 in the lowest-AOD cases to around 0.25 when the AOD is 0.3 or higher. Again, further evaluation is required to quantify performance more robustly.

The MODIS C6 ocean AE has not yet been validated thoroughly, but the errors in the SOAR VIIRS data are in-line with analyses of C5 MODIS data (Schutgens et al., 2013), and the SOAR VIIRS bias appears to be smaller. A preliminary validation of the MODIS C6 AE (Levy et al., 2013) suggested an EE for that parameter of around 0.45 and similar performance for C5 and C6; hence, the SOAR VIIRS AE data set is also performing similarly, or perhaps better, than the MODIS products. This comparison also highlights the fact that the choice of aerosol optical model seems fairly robust (i.e., the dust model is selected predominantly when the MAN AE is lower and the fine-dominated model when the MAN AE is higher). It should be noted that, particularly as AOD decreases,

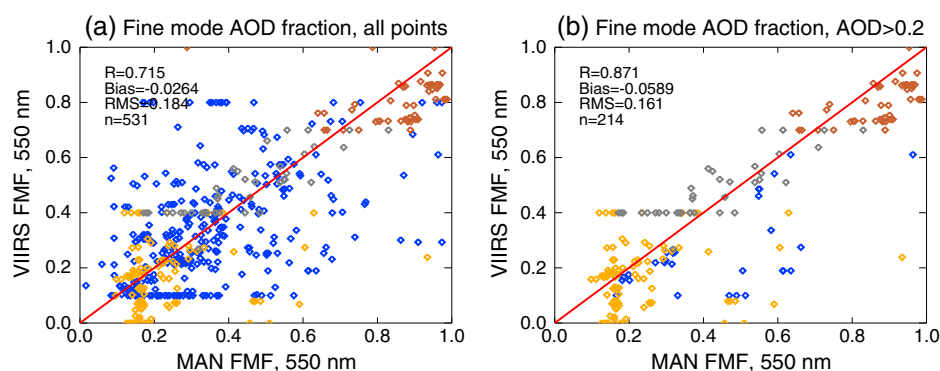


Figure 8. Scatterplots comparing VIIRS and MAN FMF at 550 nm. The comparison for (a) all points and (b) for only those points where the MAN AOD is at least 0.2. Points where the majority of VIIRS retrievals selected the dust model are shown in orange, fine dominated in brown, maritime in blue, and mixed in dark gray.

the uncertainty on AE estimated from Sun photometers can be significant, since it is the gradient between two (often small) numbers (Wagner & Silva, 2008). As a result the AE comparison in low-AOD conditions cannot be considered as strongly a validation as the AERONET/MAN data can no longer be considered a ground truth.

AERONET and MAN also apply a spectral deconvolution algorithm (SDA) to the direct-Sun AOD, which makes assumptions about the spectral dependence of fine- and coarse-mode aerosol extinction to estimate the relative fine- and coarse-mode contributions to total AOD at a wavelength of 500 nm (O'Neill et al., 2001, 2003, 2006). The uncertainty on FMF estimated by this method is variable (dependent on AOD and the true microphysical aerosol properties) but of order 0.1 (O'Neill et al., 2001), so this cannot be considered a validation to the same extent as the direct-Sun AOD comparison. The SDA FMF is compared to the FMF from the SOAR algorithm in Figure 8; the data volume is smaller than that of Figure 6 because of additional quality checks, which are part of the SDA processing (to remove cases where the assumptions made in the SDA may not be valid). Note that the MAN FMF has been converted from 500 to 550 nm to match the SOAR data, using the fine-mode and total AOD and AE within the MAN SDA product. This interpolation adds negligible additional uncertainty.

The comparison reveals a high level of agreement between the two data sets, with essentially no bias and an RMS error of 0.184. The RMS error decreases to 0.161 if only those points where MAN AOD is at least 0.2 are considered (a little under half of the points), which is as expected since the sensitivity to aerosol size increases as the AOD increases. Note that this AOD filtering removes the bulk of points where the maritime model is chosen by the retrieval, which is expected, because the typical AOD in unpolluted maritime conditions is somewhat lower than 0.2 (e.g., Smirnov et al., 2009). The MODIS C6 ocean FMF has not been evaluated, although an analysis of a previous MODIS data version by Kleidman et al. (2005) indicated that MODIS had a lower dynamic range of FMF compared to SDA data and a slightly weaker correlation (0.73 when filtered for data with AOD > 0.1, compared with 0.72 for all points here, and 0.87 for AOD > 0.2). It therefore seems likely that SOAR applied to VIIRS is performing with similar or better quality than MODIS products, which is

consistent with the AOD/AE analysis. Figure 9 shows a gradual decrease in FMF error with increasing AOD, from around 0.3 in low-AOD conditions to 0.15 when AOD is approximately 0.1 or more, again fairly consistent with the AE analysis.

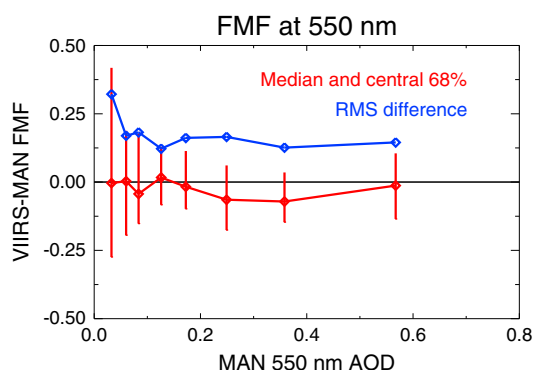


Figure 9. As in Figure 7 except for FMF.

Extending the SDA comparison to a deeper level, Figure 10 compares the fine-mode and coarse-mode AODs estimated using this technique with those from VIIRS. Given the aforementioned typical level of uncertainty on SDA FMF of order 0.1, this figure includes an estimate of the MAN fine/coarse-mode AOD uncertainty of 10% of the total AOD at 550 nm (or the calibration uncertainty of 0.02, whichever is larger). Overall, 67% of fine-mode AOD and 52% of coarse-mode AOD points match within the calculated MAN uncertainty. The SOAR-derived uncertainty on fine/coarse-mode AOD is likely to be similar to or larger than these MAN uncertainties, although as part of the purpose of this comparison

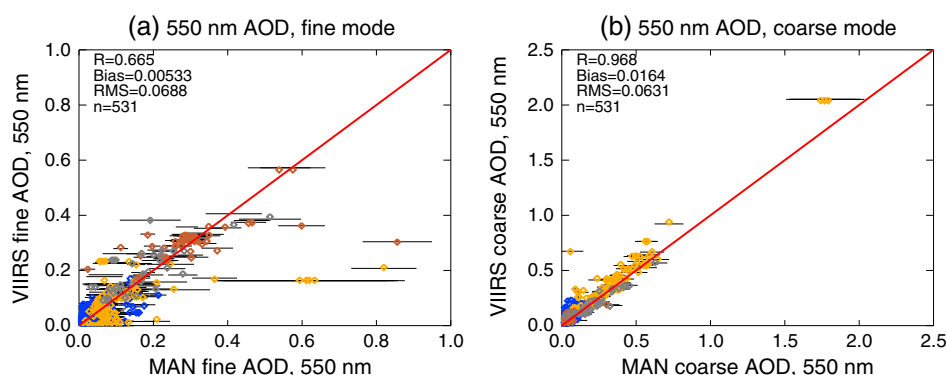


Figure 10. Scatterplots comparing VIIRS and MAN (a) fine- and (b) coarse-mode AOD at 550 nm. Comparison statistics are given in each panel. Horizontal bars provide an estimated uncertainty on the MAN data, as discussed in the text. Points where the majority of VIIRS retrievals selected the dust model are shown in orange, fine dominated in brown, maritime in blue, and mixed in dark gray.

is to assess this and to avoid overloading the figure, there is no attempt to show it on Figure 10. The coarse-mode AOD statistics is very similar to those for total AOD (Figure 6), probably because most points are either open ocean or dust dominated, in which cases the majority of the aerosol extinction is likely to be from coarse-mode particles. The correlation for fine-mode AOD is lower (0.67); the lower correlation is due in part to the smaller dynamic range for the fine-mode data. A few outliers where VIIRS retrieves significantly lower fine-mode AOD than the MAN SDA product estimate also contribute to this. Examining these cases individually reveals these to mainly be from dust storms; the ~ 0.1 uncertainty in MAN FMF for these high-AOD cases contributes a comparatively large uncertainty in fine-mode AOD. Interestingly, the median bias in fine-mode AOD (0.005) is around a third of that in coarse-mode AOD (0.016), suggesting that the positive bias in total AOD (0.013, Figure 6, although note the different sample size) may be mainly dominated by too much extinction from the coarse mode. Examining spectral AOD, Sayer, Hsu, Bettenhausen, et al. (2017) found larger bias in VIIRS data at swIR wavelengths than in the midvisible, also consistent with the possibility that the coarse-mode aerosol extinction is too large.

A larger-scale comparison against AERONET will be performed in the future to provide more robust statistics. In addition to the analysis here, preliminary validation against AERONET has been performed at predominantly low-AOD locations by Sayer, Hsu, Bettenhausen, et al. (2017) and over select dust-dominated sites by Lee et al. (2017), in analyses of sensor calibration and the importance of aerosol particle shape assumptions for mineral dust optical models, respectively.

4.2. East-West Swath Side Comparison

With a swath width of 3,040 km there is overlap between consecutive VIIRS daytime orbits, even at equatorial latitudes. This enables self-consistency checks by comparing data from the western side of the swaths with data collected on the following orbit, approximately 100 min later, from the eastern side of the swath. The two sides observe at different geometries, leading to different relative strengths of surface, aerosol, and Rayleigh signals. This analysis has been performed using data from the years 2014–2015; AOD and AE retrievals passing QA checks were separated according to whether they were to the east or west of the subsatellite point and then gridded to 1° horizontal resolution on a daily basis, requiring at least 10 retrievals on a grid cell in a given day to be considered valid, to decrease sampling-related differences, which can be nonnegligible (e.g., Sayer, Thomas, Palmer, et al., 2010). This resulted in around 2.6 million grid cells with data from eastern and western orbit halves on the same day. Due to the shape of the Earth and the S-NPP orbit, comparatively more of the overlapping data comes from midlatitude and high latitude (where the fraction of overlap between consecutive orbits' swaths is higher) than the tropics.

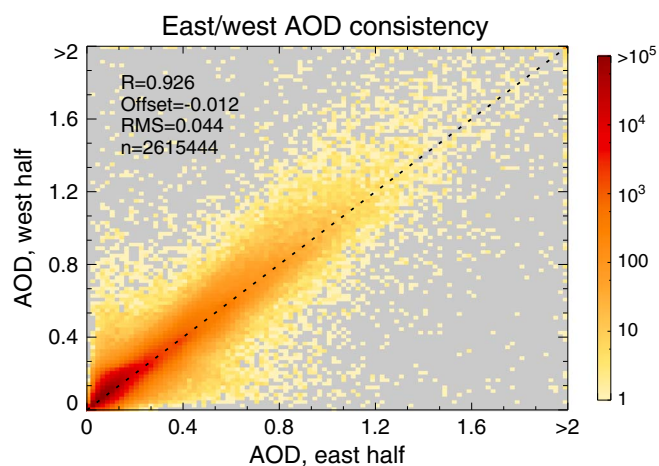


Figure 11. Scatter density histogram of matched daily 1° AOD from eastern and western swath edges during the years 2014–2015. R indicates Pearson's correlation coefficient, the offset is the median east-west AOD, RMS the root-mean-square difference, and n the number of points. Note that points with AOD > 2 are truncated along the axes, but exact values were used for the computation of all statistics.

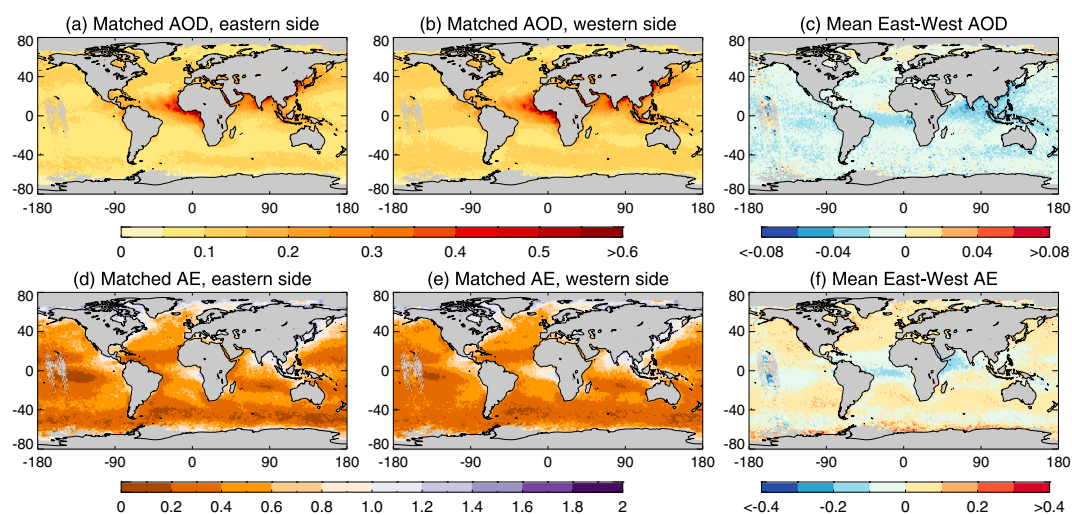


Figure 12. Comparisons between AOD (Figures 12a–12c) and AE (Figures 12d–12f) retrieved on the (a, d) eastern and (b, e) western edges (see text) of the VIIRS swath and (c, f) their difference. Data shown are a composite for the years 2014–2015. Grid cells with fewer than five valid days contributing are shaded in gray.

Figure 11 presents a scatter density histogram of the collated AOD data. As this is on a logarithmic scale, the small number of extreme outliers appears prominent than they are in absolute terms in the data. Examination of several cases reveals that these are mostly due to residual sampling differences, as in the time between consecutive orbits aerosol and cloud features move. A map of the average AOD and AE, and their difference, from both sides of the swath is shown in Figure 12. The overall spatial patterns are similar between the two halves, and in-line with expected patterns based on other data sets (e.g., Levy et al., 2013). Note that the gap in coverage in the equatorial Pacific is due to the interplay of the orbital repeat cycle with the international date line meaning that consecutive orbits are often from different dates, so not directly compared using this approach.

For AOD, the high correlation (0.926) and low RMS (0.044) on the daily data illustrate a high degree of correspondence (i.e., the level of east/west self-consistency is similar to the level of consistency with MAN; the statistics are not quite directly comparable due to sampling differences). The global median offset is -0.012 . Over most of the open ocean, the AOD on the eastern side of the swath is slightly lower than the western; in the Arctic Ocean and some dust outflow regions, the converse is true. Conversely, the eastern AE is often larger than the western AE, although there are patches where it tends to be slightly smaller. On global average, the correlation between gridded AE data from the two halves of the swath is 0.86, the median (east-west) offset 0.003 (i.e., negligible difference) and RMS 0.25. For the gridded data, for those cells with data the magnitude of the AOD differences is smaller than 0.02 in 77% of cases and smaller than 0.04 in 98% of cases. For AE, the proportions are 85% of cases within 0.1 and 98% within 0.2. The larger negative AOD differences tend to be in tropical aerosol outflow regions associated with mixed aerosol types, such as African dust/smoke, the northern Indian Ocean, and coastal eastern Asia; these differences fall within the range 0.02–0.06 and tend to correspond to the regions where eastern AE is smaller than western AE.

In a sense these differences can be considered similar to the minimum which would be expected from a comparison of any two nonsimultaneous data sets, in that the sensor and algorithm are the same, the only differences being the solar/view geometry and ~ 100 min differences in observation time. Quantifying individual contributions to the difference is difficult to do with confidence. They are likely due to a combination of sensor calibration and radiative transfer limitations (in, e.g., atmospheric or surface modeling). An additional factor might be differential sensitivity to cirrus clouds at the different viewing geometries, which may lead to different cloud masking or biases in the tropics, in particular (e.g., Huang et al., 2013). The scatter between the two will also reflect real changes in the aerosol (due to motion, emission, deposition, or aging), although these are expected to be small and on average unbiased due to the fairly short time difference between consecutive orbits. Changes in cloud populations (e.g., in rapidly changing open-celled stratocumulus) may also affect real or retrieved aerosol behavior. However, as the differences illustrated here are somewhat smaller than retrieval

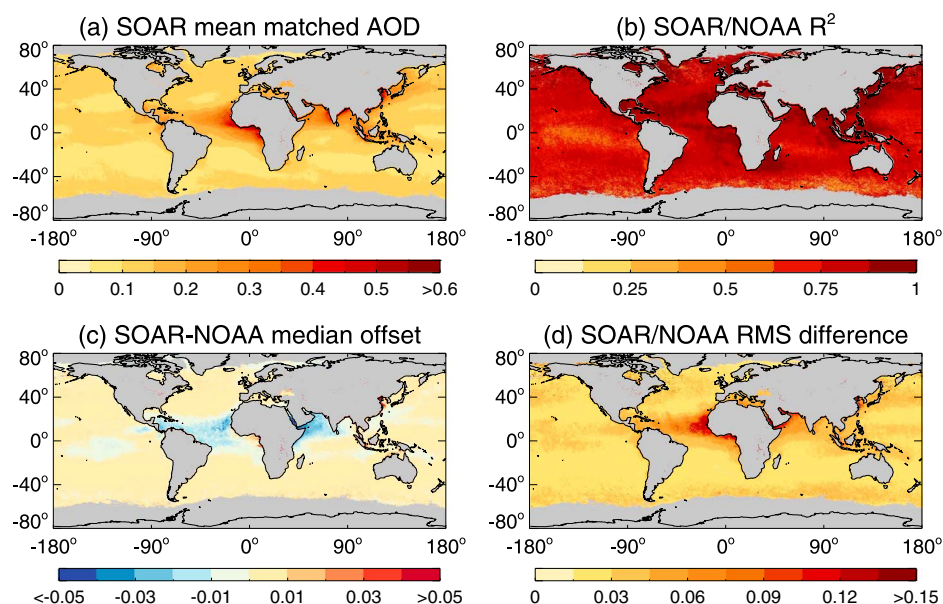


Figure 13. Comparison between SOAR and NOAA AOD from S-NPP VIIRS for 2014–2015. (a) The mean SOAR AOD for matched days, (b) the coefficient of determination between SOAR and NOAA data, (c) the median SOAR-NOAA offset, and (d) the RMS difference between daily AOD fields for each grid cell. Grid cells with fewer than 30 valid days contributing are shaded in gray.

uncertainty, and this comparison (by necessity) is only able to examine the most extreme viewing geometries, it appears that the data are sufficiently self-consistent for most applications.

4.3. Comparison With NOAA VIIRS AOD

As noted previously, NOAA also performs AOD retrievals from S-NPP measurements (Jackson et al., 2013). This section provides a brief comparison between NOAA and SOAR AOD over ocean. NOAA retrievals are also at nominal $6 \times 6 \text{ km}^2$, although granule size is different; thus, this comparison uses NOAA's daily gridded AOD product, which reports mean AOD at 550 nm 0.25° resolution on a daily basis. For this purpose, SOAR retrievals for 2014–2015 have been averaged to the same grid and a comparison made using those grid cells on a daily basis where both NOAA and SOAR products have at least three valid retrievals contributing to the average AOD within the 0.25° grid cell. Note that NOAA does not provide other gridded products like FMF or AE so no comparison of those is made here.

Mapped comparison statistics is shown in Figure 13. At least 30 days of data are required for a grid cell to be valid, in order to increase the robustness of the statistics. On the whole, the two appear very similar: for the vast majority of grid cells, the median offset between the two is smaller than 0.01 and the RMS difference in the range 0.015–0.045, with typical coefficients of determination greater than 0.5. This level of agreement is strong given the expected level of uncertainty on the AOD retrievals, that is, $\pm(0.03 + 10\%)$ for SOAR, and probably arises since the two data sets are using many of the same source measurements and have some commonalities in algorithm (so they are not entirely independent).

Larger differences are found in two main regions. The first is dust outflow from North Africa and the Arabian Peninsula, where SOAR AOD is lower. This is consistent with the fact that the NOAA algorithm does not include nonspherical dust aerosol models (Jackson et al., 2013), which results in characteristic overestimates of AOD and AE in these cases (e.g., Huang et al., 2016; Lee et al., 2017). In contrast, although more evaluation is required, SOAR does not appear to suffer from this (cf. Figure 6 and Lee et al., 2017). It is therefore likely that SOAR data are more reliable in these situations. SOAR AOD tends to be higher than NOAA retrievals in turbid/shallow waters such as central African lakes and the Yellow and Bohai Seas near China. This is likely to be related to SOAR using the backup four-band retrieval in these cases due to the turbidity; the NOAA algorithm attempts no retrievals in pixels it deems sufficiently turbid, which may cause sampling differences in these grid cells. It is not clear from this comparison whether SOAR or the NOAA data set provides more accurate

results in these areas, although as R^2 remains high and the RMS difference fairly low, it is possible that these differences (of order 0.03–0.05) are largely an offset rather than a significantly different representation of the seasonal cycle.

Validation of the NOAA product indicates an average over-water bias in AOD of order 0.025 (Huang et al., 2016), approximately 0.01 more positive than the SOAR-MAN comparison. Additionally, Huang et al. (2016) report somewhat larger errors in AE (bias of 0.12 and total uncertainty 0.57, after filtering to remove points where AOD < 0.15) than found for SOAR (Figure 7). However, Huang et al. (2016) did not provide a breakdown of site-specific results, and the AERONET comparison by nature focuses on coastal and island regions while MAN is more weighted toward the open ocean (although it does include some coastal data, dependent on cruise tracks). Thus, the two sets of metrics may not be directly comparable if the error characteristics of the data are not the same in open versus coastal waters. Future evaluation of SOAR will assess the performance of the full and backup retrieval algorithms separately.

5. Perspective and Next Steps

The bulk of the effort in the first version of the VIIRS Deep Blue data set has focused in adapting the over-land Deep Blue algorithms (Hsu et al., 2013) and over-water SOAR algorithm (Sayer, Hsu, Bettenhausen, Ahmad, et al., 2012) from MODIS, SeaWiFS, and AVHRR to VIIRS. As the sensors have similar (but not identical) spectral and spatial characteristics the same techniques for AOD retrieval have been found to be effective, although sometimes specific aspects require alterations. The VIIRS sensor offers some improvements over SeaWiFS, in particular, in regard to spatial resolution, swath width, and spectral range. The over-ocean AOD products have benefited from EOS-era experience, as well as new improvements to the algorithm (e.g., nonspherical dust aerosol models and use of cell median rather than mean AOD to reduce susceptibility to small amounts of cloud contamination within the L2 data). The result of this effort is a new NASA VIIRS AOD product with quality comparable to or better than EOS-era products generated from MODIS, SeaWiFS, and AVHRR (Levy et al., 2013; Sayer, Hsu, Bettenhausen, Ahmad, et al., 2012; Sayer, Hsu, Lee, et al., 2017). This study has introduced the over-water portion of version 1 of this new data set and provided an initial evaluation; due to space concerns, the analysis is necessarily limited in scope and additional validation and intersensor comparisons (against AERONET coastal/island sites and other satellite products) will be performed in the future.

Looking forward, there are several enhancements that will be tested for future VIIRS Deep Blue data releases, many of which could be applied to future MODIS/SeaWiFS data reprocessings as well. For example, L3 data could be generated at additional resolutions or the feasibility of changing the L2 data aggregation resolution could be investigated. Further improvements will expand the range of aerosol optical models available, to include properties typical of smoke from different global source regions (Sayer, Hsu, et al., 2014), as well as other aerosols such as volcanic ash. The ability of sensors like VIIRS to distinguish between aerosols of different compositions is limited, but SOAR could be enhanced by the inclusion of shorter-wavelength channels (e.g., 412 and 443 nm, common to SeaWiFS, MODIS, and VIIRS), where differential strength of absorption by different aerosol types can help. However, shorter wavelengths become increasingly more sensitive to aerosol vertical distribution and so some additional constraints on that, for example, based on Winker et al. (2013), would be required; ocean color variations also have a more pronounced effect in these bands. Thermal infrared measurements could also be useful for this, although are missing from SeaWiFS, and the thermal signature of aerosols is generally negligible except for mineral dust and volcanic ash under normal circumstances (because most aerosols have small infrared extinction and are located close to the surface, limiting thermal contrast).

As noted earlier, these aerosol optical model names are human-assigned interpretive types and should not be taken as definitive statements of aerosol chemical composition or source origin. The directly retrieved and derived quantities (e.g., AOD, FMF, and AE) may be more informative in terms of aiding judgment of likely contributing aerosol sources to a particular scene. However, expanding the suite of optical models will allow the retrieval to explore a richer subset of parameter space (i.e., particle size/shape and refractive index) and so potentially decrease the uncertainty on these retrieved quantities.

Other targets include the generation of additional LUTs with lower surface pressures, to more accurately model reflectance for elevated inland lakes. Although a small effect on a global scale, this may increase the utility of the data for certain regional studies. Another step is to further develop and apply techniques using VIIRS band M09 (near 1.38 μm) to identify and correct for optically thin cirrus clouds; Lee et al. (2013) illustrate

this methodology for MODIS retrievals over ocean, which can decrease AOD error from undetected cirrus clouds, as well as increase data coverage in regions of frequent cirrus occurrence such as the global tropics (as pixels can be corrected rather than discarded).

The continual evaluation of the data against resources such as AERONET and MAN, as well as field campaign data, will be performed to more robustly quantify retrieval errors and contextual biases (e.g., Zhang & Reid, 2006) and build a prognostic AOD error model as has been done for MODIS Deep Blue data (Sayer et al., 2013; Sayer, Hsu, Bettenhausen, Jeong, et al., 2015). When the reliability of AOD, AE, and the aerosol optical model selection has been more broadly established, then the range of data products derived from them could be extended to provide additional information of interest (e.g., spectral fine/coarse partition of AOD; spectral SSA), with appropriate caveats.

Although future improvements have been identified, this study has illustrated the adaptation and improvement of SOAR from SeaWiFS to VIIRS measurements. The data from this SOAR VIIRS version 1 data set are of similar quality of EOS-era products, suitable for quantitative use in scientific studies, demonstrating the fidelity of S-NPP VIIRS for continuing and enhancing the DMSP and EOS-era data records.

References

- Abdou, W. A., Martonchik, J. V., Kahn, R. A., West, R. A., & Diner, D. J. (1997). A modified linear-mixing method for calculating atmospheric path radiances of aerosol mixtures. *Journal of Geophysical Research*, 102(D14), 16,333–16,888. <https://doi.org/10.1029/96JD03434>
- Ahmad, Z., Franz, B. A., McClain, C. R., Kwiatkowska, E. J., Werdell, J., Shettle, E. P., & Holben, B. N. (2010). New aerosol models for the retrieval of aerosol optical thickness and normalized water-leaving radiances from the SeaWiFS and MODIS sensors over coastal regions and open oceans. *Applied Optics*, 49(29), 5545–5560. <https://doi.org/10.1364/AO.49.005545>
- Amante, C., & Eakins, B. W. (2009). ETOPO1 1 arc-minute global relief model: Procedures, data sources and analysis NOAA technical memorandum NESDIS NGDC-24, National Geophysical Data Center, NOAA. <https://doi.org/10.7289/V5C8276M>
- Anderson, T. L., Charlson, R. J., Winker, D. M., Ogren, J. A., & Holmén, K. (2003). Mesoscale variations of tropospheric aerosols. *Journal of the Atmospheric Sciences*, 60(1), 119–136. [https://doi.org/10.1175/1520-0469\(2003\)060<0119:MVOTA>2.0.CO;2](https://doi.org/10.1175/1520-0469(2003)060<0119:MVOTA>2.0.CO;2)
- Austin, R. W. (1974). The remote sensing of spectral radiance from below the ocean surface. In N. G. Jerlov & E. S. Nielsen (Eds.), *Optical Aspects of Oceanography* (pp. 317–344). London: Academic Press.
- Cao, C., De Luccia, F. J., Xiong, X., Wolfe, R., & Weng, F. (2014). Early on-orbit performance of the Visible Infrared Imaging Radiometer Suite onboard the Suomi National Polar-Orbiting Partnership (S-NPP) satellite. *IEEE Transactions on Geoscience and Remote Sensing*, 52(2), 1142–1156. <https://doi.org/10.1109/TGRS.2013.2247768>
- Cao, C., Xiong, J., Blonski, S., Liu, Q., Uprety, S., Shao, X., ... Weng, F. (2013). Suomi NPP VIIRS sensor data record verification, validation, and long-term performance monitoring. *Journal of Geophysical Research: Atmospheres*, 118, 11,664–11,678. <https://doi.org/10.1002/2013JD020418>
- Cox, C., & Munk, W. (1954a). Measurement of the roughness of the sea surface from photographs of the Sun's glitter. *Journal of the Optical Society of America*, 44, 838–850. <https://doi.org/10.1364/JOSA.44.000838>
- Cox, C., & Munk, W. (1954b). Statistics of the sea surface derived from Sun glitter. *Journal of Marine Research*, 13, 198–227.
- Eck, T. F., Holben, B. N., Reid, J. S., Dubovik, O., Smirnov, A., O'Neill, N. T., ... Kinne, S. (1999). Wavelength dependence of the optical depth of biomass burning, urban, and desert dust aerosols. *Journal of Geophysical Research*, 104(D24), 31,333–31,349. <https://doi.org/10.1029/1999JD009023>
- Ginoux, P., Garbuzov, D., & Hsu, N. C. (2010). Identification of anthropogenic and natural dust sources using Moderate Resolution Imaging Spectroradiometer (MODIS) Deep Blue level 2 data. *Journal of Geophysical Research*, 115, D05204. <https://doi.org/10.1029/2009JD012398>
- Hasekamp, O. P., & Landgraf, J. (2007). Retrieval of aerosol properties over land surfaces: Capabilities of multi-viewing-angle intensity and polarization measurements. *Applied Optics*, 46(16), 3332–3344. <https://doi.org/10.1364/AO.46.003332>
- Hess, M., Koepke, P., & Schult, I. (1998). Optical properties of aerosols and clouds: The software package OPAC. *Bulletin of the American Meteorological Society*, 79(5), 831–944. [https://doi.org/10.1175/1520-0477\(1998\)079](https://doi.org/10.1175/1520-0477(1998)079)
- Hsu, N. C., Jeong, M.-J., Bettenhausen, C., Sayer, A. M., Hansell, R., Seftor, C. S., ... Tsay, S.-C. (2013). Enhanced Deep Blue aerosol retrieval algorithm: The second generation. *Journal of Geophysical Research: Atmospheres*, 118, 9296–9315. <https://doi.org/10.1002/jgrd.50712>
- Hsu, N. C., Lee, J., Sayer, A. M., Carletta, N., Chen, S.-H., Tucker, C. J., ... Tsay, S.-C. (2017). Retrieving near-global aerosol loading over land and ocean from AVHRR. *Journal of Geophysical Research: Atmospheres*, 122, 9968–9989. <https://doi.org/10.1002/2017JD026932>
- Hsu, N. C., Tsay, S.-C., King, M. D., & Herman, J. R. (2004). Aerosol properties over bright-reflecting source regions. *IEEE Transactions on Geoscience and Remote Sensing*, 42(3), 557–569. <https://doi.org/10.1109/TGRS.2004.824067>
- Hu, C., Lee, Z., & Franz, B. (2012). Chlorophyll a algorithms for oligotrophic oceans: A novel approach based on three-band reflectance difference. *Journal of Geophysical Research*, 117, C01011. <https://doi.org/10.1029/2011JC007395>
- Huang, J., Hsu, N. C., Tsay, S.-C., Liu, Z., Jeong, M. J., Hansell, R. A., & Lee, J. (2013). Use of spaceborne lidar for the evaluation of thin cirrus contamination and screening in the Aqua MODIS collection 5 aerosol products. *Journal of Geophysical Research: Atmospheres*, 118, 6444–6453. <https://doi.org/10.1002/jgrd.50504>
- Huang, J., Kondragunta, S., Laszlo, I., Liu, H., Remer, L. A., Zhang, H., ... Petrenko, M. (2016). Validation and expected error estimation of Suomi-NPP VIIRS aerosol optical thickness and Ångström exponent with AERONET. *Journal of Geophysical Research: Atmospheres*, 121, 7139–7360. <https://doi.org/10.1002/2016JD024834>
- Hyer, E. H., Reid, J. S., & Zhang, J. (2011). An over-land aerosol optical depth data set for data assimilation by filtering, correction, and aggregation of MODIS Collection 5 optical depth retrievals. *Atmospheric Measurement Techniques*, 4, 379–408. <https://doi.org/10.5194/amt-4-379-2011>
- Jackson, J. M., Liu, H., Laszlo, I., Kondragunta, S., Remer, L. A., Huang, J., & Huang, H.-C. (2013). Suomi-NPP VIIRS aerosol algorithms and data products. *Journal of Geophysical Research: Atmospheres*, 118, 12,673–12,689. <https://doi.org/10.1002/2013JD020449>

Acknowledgments

Further information about Deep Blue is available at <https://deepblue.gsfc.nasa.gov>. This research was funded under the Suomi NPP program. The MAN cruise Pls (A. Baker, S. Bilanger, R. Brewin, S. Broccardo, Y. Courcoux, P. Disterhoff, F. Dulac, R. Dunn, H. Evangelista, H. Findlay, R. Frouin, J. I. Goes, M. Harvey, M. Heller, B. N. Holben, L. Istomina, E. Joseph, P. Kermen, S. Kinne, I. Koren, N. Lagrosas, W. Landing, E. Lewis, H. S. Lim, E. Lobecker, A. Mannino, L. McKenna, N. Nalli, N. Nelson, M. Ondrusek, N. Pahlevan, P. Quinn, V. Radionov, J. S. Reid, C. Roman, J. Sciare, A. Skarke, V. Slabakova, T. Smyth, D. Sowers, M. Tzortziou, G. Stenchikov, L. Yurganov, G. Zibordi, Yanto, and T. Zielinski) are thanked for the creation and stewardship of the Sun photometer data records. AERONET and MAN data are available from <https://aeronet.gsfc.nasa.gov>. The GEOS-5 data used in this study have been provided by the Global Modeling and Assimilation Office (GMAO) at NASA Goddard Space Flight Center (<https://gmao.gsfc.nasa.gov>). NOAA VIIRS aerosol data were obtained from https://www.star.nesdis.noaa.gov/smcd/emb/viirs_aerosol. D. Antoine (Curtin), B. A. Franz (NASA GSFC), Z. Lee (University of Massachusetts Boston), and A. Vasilkov (SSAI) are thanked for useful discussions about the current status of measurements of the optical properties of seawater and bidirectional aspects of remote sensing reflectance and R. Spurr (RT Solutions) for additional development of the VLIDORT RT code and interface. Data processing was facilitated by use of the GNU Parallel utility by Tange (2011). The Atmospheres SIPs at the University of Wisconsin (particularly S. Dutcher) are acknowledged for data hosting and provision and assistance with computational resources. Prior to the public release of the VIIRS Deep Blue aerosol products, example demonstration data are available from the authors upon request. Three anonymous reviewers are thanked for their comments, which helped to improve the clarity of this manuscript and spurred the inclusion of some additional analyses.

- Kahn, R. A., Garay, M. J., Nelson, D. L., Levy, R. C., Bull, M. A., Diner, D. J., ... Tanré, D. (2011). Response to "Toward unified satellite climatology of aerosol properties: 3. MODIS versus MISR versus AERONET". *Journal of Quantitative Spectroscopy and Radiative Transfer*, 112(5), 901–909. <https://doi.org/10.1016/j.jqsrt.2010.11.001>
- Kleidman, R. G., O'Neill, N. T., Remer, L. A., Kaufman, Y. J., Eck, T. F., Tanré, D., ... Holben, B. N. (2005). Comparison of Moderate Resolution Imaging Spectroradiometer (MODIS) and Aerosol Robotic Network (AERONET) remote-sensing retrievals of aerosol fine mode fraction over ocean. *Journal of Geophysical Research*, 110, 10,111–10,124. <https://doi.org/10.1029/2005JD005760>
- Knobelspiesse, K. D., Pietras, C., Fargion, G. S., Wang, M., Frouin, R., Miller, M. A., ... Balch, W. M. (2004). Maritime aerosol optical thickness measured by handheld Sun photometers. *Remote Sensing of Environment*, 93(1–2), 87–106. <https://doi.org/10.1016/j.rse.2004.06.018>
- Koepeke, P. (1984). Effective reflectance of oceanic whitecaps. *Applied Optics*, 23(11), 1816–1824. <https://doi.org/10.1364/AO.23.001816>
- Koren, I., Kaufman, Y., Washington, R., Todd, M. C., Rudich, Y., Martins, J. V., & Rosenfeld, D. (2006). The Bodélé depression: A single spot in the Sahara that provides most of the mineral dust to the Amazon forest. *Environmental Research Letters*, 1, 14005. <https://doi.org/10.1088/1748-9326/1/1/014005>
- Lee, J., Hsu, N. C., Bettenhausen, C., & Sayer, A. M. (2013). Retrieval of aerosol optical depth under thin cirrus from MODIS: Application to an ocean algorithm. *Journal of Geophysical Research: Atmospheres*, 118, 10,111–10,124. <https://doi.org/10.1002/jgrd.50806>
- Lee, J., Hsu, N. C., Sayer, A. M., Bettenhausen, C., & Yang, P. (2017). AERONET-based nonspherical dust optical models and effects on the VIIRS Deep Blue/SOAR over water aerosol product. *Journal of Geophysical Research: Atmospheres*, 122, 10,384–10,401. <https://doi.org/10.1002/2017JD027258>
- Lee, J., Kim, J., Yang, P., & Hsu, N. C. (2012). Improvement of aerosol optical depth retrieval from MODIS spectral reflectance over the global ocean using new aerosol models archived from AERONET inversion data and tri-axial ellipsoidal dust database. *Atmospheric Chemistry and Physics*, 12, 7087–7102. <https://doi.org/10.5194/acp-12-7087-2012>
- Lee, T. E., Miller, S. D., Turk, F. J., Schueler, C., Julian, R., Deyo, S., ... Wang, S. (2006). The NPOESS VIIRS Day/Night visible sensor. *Bulletin of the American Meteorological Society*, 87, 191–199. <https://doi.org/10.1175/BAMS-87-2-191>
- Lei, N., & Xiong, X. (2017). Products of the SNPP VIIRS SD screen transmittance and the SD BRDFs from both yaw maneuver and regular on-orbit data. *IEEE Transactions on Geoscience and Remote Sensing*, 55(4), 1975–1987. <https://doi.org/10.1109/TGRS.2016.2633967>
- Levenberg, K. (1944). A method for the solution of certain non-linear problems in least-squares. *Quarterly of Applied Mathematics*, 2(2), 164–168. <https://doi.org/10.1090/qam/10666>
- Levy, R. C., Mattoo, S., Munchak, L. A., Remer, L. A., Sayer, A. M., Patadia, F., & Hsu, N. C. (2013). The Collection 6 MODIS aerosol products over land and ocean. *Atmospheric Measurement Techniques*, 6, 2989–3034. <https://doi.org/10.5194/amt-6-2989-2013>
- Levy, R. C., Remer, L. A., Mattoo, S., Vermote, E. F., & Kaufman, Y. J. (2007). Second-generation operational algorithm: Retrieval of aerosol properties over land from inversion of Moderate Resolution Imaging Spectroradiometer spectral reflectance. *Journal of Geophysical Research*, 112, D13211. <https://doi.org/10.1029/2006JD007811>
- Li, R.-R., Kaufman, Y. J., Gao, B.-C., & Davis, C. O. (2003). Remote sensing of suspended sediments and shallow coastal waters. *IEEE Transactions on Geoscience and Remote Sensing*, 41(3), 559–566. <https://doi.org/10.1109/TGRS.2003.810227>
- Li, Z., Zhao, X., Kahn, R., Mishchenko, M., Remer, L., Lee, K.-H., ... Maring, H. (2009). Uncertainties in satellite remote sensing of aerosols and impact on monitoring its long-term trend: A review and perspective. *Annales de Geophysique*, 27, 2755–2770. <https://doi.org/10.5194/angeo-27-2755-2009>
- Liu, H., Remer, L. A., Huang, J., Huang, H.-C., Kondragunta, S., Laszlo, I., ... Jackson, J. M. (2014). Preliminary evaluation of S-NPP VIIRS aerosol optical thickness. *Journal of Geophysical Research: Atmospheres*, 119, 3942–3962. <https://doi.org/10.1002/2013JD020360>
- Lyapustin, A., Wang, Y., Laszlo, I., Kahn, R., Korkin, S., Remer, L., ... Reid, J. S. (2011). Multiangle implementation of atmospheric correction (MAIAC): 2. Aerosol algorithm. *Journal of Geophysical Research*, 116, D03211. <https://doi.org/10.1029/2010JD014986>
- Marquardt, D. R. (1963). An algorithm for the least-squares estimation of nonlinear parameters. *SIAM Journal of Applied Mathematics*, 11(2), 431–441. <https://doi.org/10.2307/2098941>
- Martins, J. V., Tanré, D., Remer, L., Kaufman, Y., Mattoo, S., & Levy, R. (2002). MODIS cloud screening for remote sensing of aerosols over oceans using spatial variability. *Geophysical Research Letters*, 29(12), 1619. <https://doi.org/10.1029/2001GL013252>
- Mishchenko, M. I., Geogdzhayez, I. V., Cairns, B., Rossow, W. B., & Lacis, A. A. (1999). Aerosol retrievals over the ocean by use of channels 1 and 2 AVHRR data: Sensitivity analysis and preliminary results. *Applied Optics*, 38(36), 7325–7341. <https://doi.org/10.1364/AO.38.007325>
- Mishchenko, M. I., Travis, L. D., Kahn, R. A., & West, R. A. (1997). Modeling phase functions for dustlike tropospheric aerosols using a shape mixture of randomly oriented polydisperse spheroids. *Journal of Geophysical Research*, 102(D14), 16,831–16,847. <https://doi.org/10.1029/96JD02110>
- Morel, A., & Prieur, L. (1977). Analysis of variations in ocean color. *Limnology and Oceanography*, 22(4), 709–722. <https://doi.org/10.4319/lo.1977.22.4.0709>
- O'Dowd, C. D., & de Leeuw, G. (2007). Marine aerosol production: A review of the current knowledge. *Philosophical Transactions of the Royal Society A*, 365, 1753–1774. <https://doi.org/10.1098/rsta.2007.2043>
- O'Neill, N., Eck, T., Smirnov, A., Holben, B., & Thulasiraman, S. (2006). Spectral deconvolution algorithm technical memo (Tech. Rep.): NASA Goddard Space Flight Center. revision April 26, 2006, version 4. Retrieved from http://aeronet.gsfc.nasa.gov/new_web/PDF/tauf_tauc_technical_memo1.pdf, Accessed, December 2016
- O'Neill, N. T., Dubovik, O., & Eck, T. F. (2001). Modified ångström coefficient for the characterization of submicrometer aerosols. *Applied Optics*, 40(15), 2368–2375. <https://doi.org/10.1364/AO.40.002368>
- O'Neill, N. T., Eck, T. F., Smirnov, A., Holben, B. N., & Thulasiraman, S. (2003). Spectral discrimination of coarse and fine mode optical depth. *Journal of Geophysical Research*, 108(D17), 4559–4573. <https://doi.org/10.1029/2002JD002975>
- Remer, L. A., Mattoo, S., Levy, R. C., & Munchak, L. A. (2013). MODIS 3 km aerosol product: Algorithm and global perspective. *Atmospheric Measurement Techniques*, 6, 1829–1844. <https://doi.org/10.5194/amt-6-1829-2013>
- Sayer, A. M., Hsu, N. C., & Bettenhausen, C. (2015). Implications of MODIS bow-tie distortion on aerosol optical depth retrievals, and techniques for mitigation. *Atmospheric Measurement Techniques*, 8, 5277–5288. <https://doi.org/10.5194/amt-8-5277-2015>
- Sayer, A. M., Hsu, N. C., Bettenhausen, C., Ahmad, Z., Holben, B. N., Smirnov, A., ... Zhang, J. (2012). SeaWiFS Ocean Aerosol Retrieval (SOAR): Algorithm, validation, and comparison with other data sets. *Journal of Geophysical Research*, 117, D03206. <https://doi.org/10.1029/2011JD016599>
- Sayer, A. M., Hsu, N. C., Bettenhausen, C., Holz, R. E., Lee, J., Quinn, G., & Veglio, P. (2017). Cross-calibration of S-NPP VIIRS moderate-resolution reflective solar bands against MODIS Aqua over dark water scenes. *Atmospheric Measurement Techniques*, 10, 1425–1444. <https://doi.org/10.5194/amt-10-1425-2017>
- Sayer, A. M., Hsu, N. C., Bettenhausen, C., & Jeong, M.-J. (2013). Validation and uncertainty estimates for MODIS Collection 6 "Deep Blue" aerosol data. *Journal of Geophysical Research: Atmospheres*, 118, 7864–7872. <https://doi.org/10.1002/jgrd.50600>

- Sayer, A. M., Hsu, N. C., Bettenhausen, C., Jeong, M.-J., Holben, B. N., & Zhang, J. (2012). Global and regional evaluation of over-land spectral aerosol optical depth retrievals from SeaWiFS. *Atmospheric Measurement Techniques*, 5, 1761–1778. <https://doi.org/10.5194/amt-5-1761-2012>
- Sayer, A. M., Hsu, N. C., Bettenhausen, C., Jeong, M.-J., & Meister, G. (2015). Effect of MODIS Terra radiometric calibration improvements on Collection 6 Deep Blue aerosol products: Validation and Terra/Aqua consistency. *Journal of Geophysical Research: Atmospheres*, 120, 12,157–12,174. <https://doi.org/10.1002/2015JD023878>
- Sayer, A. M., Hsu, N. C., Eck, T. F., Smirnov, A., & Holben, B. N. (2014). AERONET-based models of smoke-dominated aerosol near source regions and transported over oceans, and implications for satellite retrievals of aerosol optical depth. *Atmospheric Chemistry and Physics*, 14, 11,493–11,523. <https://doi.org/10.5194/acp-14-11493-2014>
- Sayer, A. M., Hsu, N. C., Lee, J., Carletta, N., Chen, S.-H., & Smirnov, A. (2017). Evaluation of NASA Deep Blue/SOAR aerosol retrieval algorithms applied to AVHRR measurements. *Journal of Geophysical Research: Atmospheres*, 122, 9945–9967. <https://doi.org/10.1002/2017JD026934>
- Sayer, A. M., Munchak, L. A., Hsu, N. C., Levy, R. C., Bettenhausen, C., & Jeong, M.-J. (2014). MODIS Collection 6 aerosol products: Comparison between Aqua's e-Deep Blue, Dark Target, and "merged" data sets, and usage recommendations. *Journal of Geophysical Research: Atmospheres*, 119(13,965–13,989). <https://doi.org/10.1002/2014JD022453>
- Sayer, A. M., Smirnov, A., Hsu, N. C., & Holben, B. N. (2012). A pure marine aerosol model, for use in remote sensing applications. *Journal of Geophysical Research*, 117, D05213. <https://doi.org/10.1029/2011JD016689>
- Sayer, A. M., Smirnov, A., Hsu, N. C., Munchak, L. A., & Holben, B. N. (2012). Estimating marine aerosol particle volume and number from Maritime Aerosol Network data. *Atmospheric Chemistry and Physics*, 12, 8889–8909. <https://doi.org/10.5194/acp-12-8889-2012>
- Sayer, A. M., Thomas, G. E., & Grainger, R. G. (2010). A sea surface reflectance model for (A)ATSR, and application to aerosol retrievals. *Atmospheric Measurement Techniques*, 3, 813–838. <https://doi.org/10.5194/amt-3-813-2010>
- Sayer, A. M., Thomas, G. E., Palmer, P. I., & Grainger, R. G. (2010). Some implications of sampling choices on comparisons between satellite and model aerosol optical depth fields. *Atmospheric Chemistry and Physics*, 10, 10,705–10,716. <https://doi.org/10.5194/acp-10-10705-2010>
- Schutgens, N. A. J., Nakata, M., & Nakajima, T. (2013). Validation and empirical correction of MODIS AOT and AE over ocean. *Atmospheric Measurement Techniques*, 6, 2455–2475. <https://doi.org/10.5194/amt-6-2455-2013>
- Smirnov, A., Holben, B. N., Giles, D. M., Slutsker, I., O'Neill, N. T., Eck, T. F., ... Diehl, T. L. (2011). Maritime Aerosol Network as a component of AERONET—first results and comparison with global aerosol models and satellite retrievals. *Atmospheric Measurement Techniques*, 4, 583–597. <https://doi.org/10.5194/amt-4-583-2011>
- Smirnov, A., Holben, B. N., Slutsker, I., Giles, D. M., McLain, C. R., Eck, T. F., ... Jourdain, F. (2009). Maritime aerosol network as a component of aerosol robotic network. *Journal of Geophysical Research*, 112, D06204. <https://doi.org/10.1029/2008JD011257>
- Spurr, R. J. D. (2006). VLIDORT: A linearized pseudo-spherical vector discrete ordinate radiative transfer code for forward model and retrieval studies in multilayer multiple scattering media. *Journal of Quantitative Spectroscopy and Radiative Transfer*, 102(2), 316–342. <https://doi.org/10.1016/j.jqsrt.2006.05.005>
- Stowe, L., Ignatov, A., & Singh, R. (1997). Development, validation, and potential enhancements to the second-generation operational aerosol product at NOAA/NESDIS. *Journal of Geophysical Research*, 102(D14), 16,923–16,934.
- Swap, R. J., Annegarn, H. J., Suttles, J. T., King, M. D., Platnick, S., Privette, J. L., & Scholes, R. J. (2003). Africa burning: A thematic analysis of the Southern African Regional Science Initiative (SAFARI 2000). *Journal of Geophysical Research*, 108, 8465. <https://doi.org/10.1029/2003JD003747>
- Tange, O. (2011). GNU Parallel—The command-line power tool. *The USENIX Magazine*, 36, 42–47.
- Tanré, D., Herman, M., & Kaufman, Y. J. (1996). Information on aerosol size distribution contained in solar reflected spectral radiances. *Journal of Geophysical Research*, 101(D14), 19,043–19,060. <https://doi.org/10.1029/96JD00333>
- Tanré, D., Kaufman, Y. J., Herman, M., & Mattoo, S. (1997). Remote sensing of aerosol properties over oceans using the MODIS/EOS spectral radiances. *Journal of Geophysical Research*, 102(D14), 16,971–16,988. <https://doi.org/10.1029/96JD03437>
- Várnai, T., & Marshak, A. (2009). MODIS observations of enhanced clear sky reflectance near clouds. *Geophysical Research Letters*, 36, L06807. <https://doi.org/10.1029/2008GL037089>
- Wagner, F., & Silva, A. M. (2008). Some considerations about Ångström exponent distributions. *Atmospheric Chemistry and Physics*, 8, 481–489. <https://doi.org/10.5194/acp-8-481-2008>
- Wang, J., & Martin, S. T. (2007). Satellite characterization of urban aerosols: Importance of including hygroscopicity and mixing state in the retrieval algorithms. *Journal of Geophysical Research*, 112, D17203. <https://doi.org/10.1029/2006JD008078>
- Winker, D. M., Tackett, J. L., Getzewich, B. J., Liu, Z., Vaughan, M. A., & Rogers, R. R. (2013). The global 3-D distribution of tropospheric aerosols as characterized by CALIOP. *Atmospheric Chemistry and Physics*, 13, 3345–3361. <https://doi.org/10.5194/acp-13-3345-2013>
- Wolfe, R. E., Lin, G., Nishihama, M., Tewari, K. P., & Montano, E. (2012). NPP VIIRS early on-orbit geometric performance. In *Proceedings of SPIE 8510, Earth Observing Systems XVII, 8510*, San Diego, CA, pp. 851013. <https://doi.org/10.1117/12.929925>
- Wolfe, R. E., Lin, G., Nishihama, M., Tewari, K. P., Tilton, J. C., & Isaacman, A. R. (2013). Suomi NPP VIIRS prelaunch and on-orbit geometric calibration and characterization. *Journal of Geophysical Research: Atmospheres*, 118, 11,508–11,521. <https://doi.org/10.1002/jgrd.50873>
- Xiong, X., Butler, J., Chiang, K., Efremova, B., Fulbright, J., Lei, N., ... Wu, A. (2016). Assessment of S-NPP VIIRS on-orbit radiometric calibration and performance. *Remote Sensing*, 8(2), 84. <https://doi.org/10.3390/rs8020084>
- Zhang, J., & Reid, J. S. (2006). MODIS aerosol product analysis for data assimilation: Assessment of over-ocean level 2 aerosol optical thickness retrievals. *Journal of Geophysical Research*, 111, D22207. <https://doi.org/10.1029/2005JD006898>